



UPPSALA
UNIVERSITET

Examensarbete vid Institutionen för geovetenskaper
Degree Project at the Department of Earth Sciences
ISSN 1650-6553 Nr 588

In-Situ Gold Resource Estimation Using Satellite Remote Sensing and Machine Learning in Defunct Tailing Storage Facilities (South Africa)

In-situ guldresursuppskattning med hjälp
av satellitfjärranalys och maskininlärning i
nedlagda lagringsanläggningar, Sydafrika

Shenelle Agard

In-Situ Gold Resource Estimation Using Satellite Remote Sensing and Machine Learning in Defunct Tailing Storage Facilities (South Africa)

In-situ guldresursuppskattning med hjälp
av satellitfjärranalys och maskininlärning i
nedlagda lagringsanläggningar, Sydafrika

Shenelle Agard



The work of this thesis was carried out in cooperation with Sibanye-Stillwater and Witwatersrand University.

ISSN 1650-6553

Copyright © Shenelle Agard

Published at Department of Earth Sciences, Uppsala University (www.geo.uu.se), Uppsala, 2023

Declaration

I declare that this thesis is my own original work, conducted under the supervision of Prof. Dr. Glen Nwaila and Dr. Pauline Jeanneret and mentorship of Dr. Steven Zhang and Dr. Julie E. Bourdeau (Geological Survey of Canada), and Ms. Janine Fleming (Sibanye-Stillwater). It is submitted in fulfilment of the requirements for the degree of International Master of Science in Sustainable and Innovative Natural Resource Management (SINReM) MSc at Uppsala University, Sweden. No part of this research has been submitted in the past, or is being submitted, for a degree or any examination at any other university.

Abstract

In-situ gold resource estimation using satellite remote sensing and machine learning in defunct tailing storage facilities (South Africa)

Shenelle Agard

The mining industry generates billions of tonnes of waste annually, which is often stored in tailings storage facilities (TSF). This waste is generated from the extraction of ore from surface or underground mines, as well as from metallurgical processing and low-grade stockpiles. TSF can have significant environmental impacts, as they can cause acid mine drainage resulting in the leaching and transport of heavy metals into ground and surface waters. With increasing demand for critical raw material, recent studies have shown that the valorisation of mine waste can be a potential secondary source of critical raw materials. The valorisation of mine waste is possible when the waste is accurately characterised.

A novel method that uses multispectral satellite remote sensing and machine learning to estimate the mineral resource in a defunct TSF in the Witwatersrand Basin, South Africa is proposed in this research. Four machine learning models: 1) random forest (RF); 2) adaptive boosting (AB); 3) extra trees (ET); and 4) k-nearest neighbours are developed using supervised machine learning. The models are trained using training data acquired from a TSF with known gold concentration located 3 kilometres from the TSF and deployed on the TSF to predict the gold grades.

The results of the machine learning model predictions indicates that machine learning models had high performances for predicting gold grades in the TSF. The AB, RF and ET, models performed best. Their performances were evaluated using the coefficient of determination (R^2) value. The R^2 values for the machine learning models were 0.95, 0.92, 0.87 and 0.70 for AB, ET, RF and kNN respectively. The mean gold grade predicted was 0.44 g/t by all machine learning models. This was compared to a 2D surficial geostatistical model which estimated 0.35g/t gold in the TSF using ordinary kriging and a 2D vertically averaged geostatistical model with an estimated 0.4 g/t mean gold grade. The short-wave infrared (SWIR) - band 11 at a 20 m spatial resolution had the highest correlation with the reflectance of gold in the TSF. This study demonstrated the value of leveraging multi-spectral remote sensing data and machine learning to perform mineral resource estimation in defunct TSF.

Keywords: tailings storage facility, critical raw materials, machine learning, mine valorisation

Degree Project E1 in Sustainable Innovative Natural Resource Management, 1GV193, 30 credits

Supervisors: Glen Nwaila and Pauline Jeanneret

Department of Earth Sciences, Uppsala University, Villavägen 16, SE-752 36 Uppsala (www.geo.uu.se)

ISSN 1650-6553, Examensarbete vid Institutionen för geovetenskaper, No. 588, 2023

The whole document is available at www.diva-portal.org

Popular science summary

Using satellite images to determine gold grade in abandoned mine waste dump

Shenelle Agard

Like light entering and reflecting from our eyes, allowing us to see the beauty of our world in living colours, so are the works of satellites. We do not see them, but they are hundreds, orbiting the earth daily, taking millions of photographs with their special cameras. They are Earth's best photographers. Satellites take photos of our land, oceans, atmosphere, coastal zones and forests, zooming in and out to capture details of the Earth. The photographs are cleaned to remove clouds and stored where it can be accessed and used by all of us. Google map app is one example of how we use the pictures taken by the satellites orbiting our Earth.

Abandoned mine waste dumps can cause harm to the environment when they are not constructed correctly. These waste dumps contain waste accumulated from many years of mining metals such as gold and other important metals that are used to manufacture our cellphones and important technologies such as wind turbines. When the waste is discarded in the waste dump, it may contain some of the important metals for wind turbines. As there is increasing need for these metals now and in the future, it is important that we know the quantity of important metals contained in the waste dumps. One way to do this is by using Earth's best photographers, satellites.

Satellite images of the waste dump are used to determine the amount of gold in the surface of the waste dump. Holes drilled in the waste dump helps to determine the amount of gold in the depths of the waste dump. Four (4) different computer programs go through each image which contains millions of little images that represent the waves reflected from the surface of the waste dump and groups them. The computer programs know the waves reflected by gold. As such, they identify gold in the little images. All four computer programmes identified the average mean of gold grades as 0.44 grammes per tonne. This can be compared to actual gold mines where mine waste originates. Surface mines have estimated average gold grades of 1 to 4 grams per tonne while underground mines have estimated average gold grades of 2.6 to 9.8 grammes per tonne. This differs by country. This shows that satellite images and computer programming can help to determine the amount of gold in an abandoned waste dump that is comparable to actual gold deposits globally.

Keywords: tailings storage facility, critical raw materials, machine learning, mine valorisation

Degree Project E1 in Sustainable Innovative Natural Resource Management, IGV193, 30 credits

Supervisors: Glen Nwaila and Pauline Jeanneret

Department of Earth Sciences, Uppsala University, Villavägen 16, SE-752 36 Uppsala (www.geo.uu.se)

ISSN 1650-6553, Examensarbete vid Institutionen för geovetenskaper, No. 588, 2023

The whole document is available at www.diva-portal.org

Table of Contents

| | |
|---|-----------|
| 1. Introduction..... | 1 |
| 2. Aim and Objectives..... | 3 |
| 2.1. Research questions | 3 |
| 3. Background | 4 |
| 3.1. Industry collaborator | 4 |
| 3.2. Study area..... | 4 |
| 3.2.1. Geological setting..... | 6 |
| 3.3. Previous Work..... | 8 |
| 3.3.1 Valorisation of mine tailings..... | 8 |
| 3.3.2 Satellite remote sensing in mine waste valorisation and characterization..... | 8 |
| 3.3.3 Machine Learning in mineral resource estimation..... | 9 |
| 4. Data and Methods | 12 |
| 4.1. Source of data..... | 12 |
| 4.2. Geostatistical based predictive modelling..... | 16 |
| 4.2.1. 3D Block model..... | 17 |
| 4.2.2. Variogram analysis | 18 |
| 4.2.3. 2D surficial and 2D vertically averaged geostatistical models | 19 |
| 4.3. Machine learning-based predictive modelling | 20 |
| 4.3.1. Data pre-processing | 21 |
| 4.3.2. Model training | 21 |
| 4.3.3. Model cross-validation | 23 |
| 4.3.4. Deployment | 23 |
| 5. Results | 24 |
| 5.1. Integration of geostatistical and machine learning models | 24 |
| 5.2. Transfer of machine learning models for predictive block modelling..... | 27 |
| 5.3. Sentinel-2 multi-spectral band decomposition for prediction of gold..... | 31 |
| 6. Discussion..... | 35 |
| 6.1. Evaluation of prediction efficiency and accuracy | 35 |
| 6.2. Assessment of the suitability of machine learning algorithm for spatial predictive modeling of gold in TSFs..... | 38 |
| 6.3. Efficiency of multi-spectral remote sensing band in encoding spatial features and gold concentration | 39 |
| 7. Recommendations | 40 |
| 8. Conclusion | 41 |
| 9. Acknowledgements | 43 |
| 10. References..... | 44 |

| | |
|--|-----------|
| Appendix A-Descriptive statistics plot for the resource models. (a) kNN, (b) ET, (c) RF and (d) AB. | |
| Appendix B - Histogram and descriptive statistics plot for reflectance in spectral bands 2, 3, 4, 8 and 11..... | 49 |
| Appendix C – Machine learning algorithms prediction parameters..... | 50 |
| Appendix D – 3D Block model showing boreholes drilled in Lindum TSF. | 51 |
| Appendix E – Variogram maps for bands 2, 3, 4, 8 and 11 using AB predictions | 52 |

List of Figures

| | |
|---|----|
| Figure 1. Location of the Lindum TSF in South Africa. The Lindum TSF is located at the red point. | 4 |
| Figure 2. Sections of Lindum TSF adapted from Deswick Mining Consultants (2014). | 5 |
| Figure 3. Borehole positions in sections of the TSF on top of LiDAR 3D geostatistical model. | 5 |
| Figure 4. Regional geology map of Witwatersrand Basin and surrounding area (Modified after Frimmel, 2014). | 7 |
| Figure 5 - Block diagram of the research methodology. The block diagram of the methodology followed in this research. | 16 |
| Figure 6. 3D geostatistical block model of the TSF. | 17 |
| Figure 7. Visualization of 2D vertically averaged (a) surficial (b) geostatistical model of the of the TSF, using ML overlaid on top of the satellite-borne imagery of the TSF (Zhang et al., 2022a). | 20 |
| Figure 8. ML methodology followed the steps outlined in the block diagram. Adapted from Nwaila et al., 2019. | 20 |
| Figure 9. Satellite image of Dump 20 TSF where training data was obtained from and Lindum TSF (Zhang et al., 2023a). | 22 |
| Figure 10. (a,b) ML models using the image taken on 2015-08-24. (c) Abo boosting, (d) extra trees (I, (e) random forest (RF), (f) K-nearest neighbor (kNN). Visual differences between prediction maps form ML methods and he Geostatistical models. | 25 |
| Figure 11. Histogram of predicted gold grades for the 2D geostatistical and ML models. The geostatistical model histograms both show bimodal behavior. | 26 |
| Figure 12. COD plot of ML methods for gold grade prediction in the TSF. (a) AB, (b) ET, (c) RF and (d) kNN. | 28 |
| Figure 13. Visualizations of OK gold grade estimates showing spatial continuity of the surficial gold grades. (a) AB, (b) ET, (c) RF and (d) kNN. | 29 |
| Figure 14. Experimental variogram with fitted variogram model. (a) AB, (b) kNN, (c) RF and (d) ET. | 30 |
| Figure 15. OK estimation maps for the five Bands selected. (a) Band 8, (b) Band 3, (c) Band 11 and (d) Band 4 and (e) Band 2. | 32 |
| Figure 16. A comparison of the CoD plots for the predicted gold grades and the OK gold grade estimation. | 33 |
| Figure 17. Plot of the residuals when comparing the actual and the predicted gold grades in the TSF. | 34 |
| Figure 18. Prediction maps generated using AB ML model. Progressive mining of the 1A section shows the removal of the high-grade gold tailing. | 37 |
| Figure 19. Sentinel satellite image 6 January 2015. | 38 |

List of Tables

| | |
|---|----|
| Table 1. Sentinel-2 satellite image band characteristics. | 14 |
| Table 2. Sentinel-2 images and the date of acquisition. Images acquired from 24 August 2015 to 04 October 2019. | 15 |
| Table 3. Parameter grid for employed machine learning algorithms..... | 23 |
| Table 4. Descriptive statistics of the predicted gold grades..... | 26 |
| Table 5. Comparison of CoD for the ML model prediction and the Kriged prediction values. | 27 |
| Table 6. CoD value for the comparison of the actual gold grade predictions and the OK estimations. | 31 |

Abbreviations and acronyms

AB – Adaptive Boosting

AMD – Acid mine drainage

Au - Gold

CRM – Critical raw material

CRS – Coordinate reference system

ET - Extra trees

EM – Electromagnetic waves

Fe – Iron

FLAASH - Fast line-of-sight atmospheric analysis of spectral hypercubes

g/t – Grams per tonne

kNN – K-nearest neighbor

Ma – Millions of years

MSI - Multispectral instrument

ML – Machine learning

OK – Ordinary Kriging

PGM – Platinum group metals

REEs – Rare earth elements

RF - Random Forest

SDGs – Sustainable development goals

SWIR - Shortwave infrared

TOA - Top of the atmosphere

TSF - Tailing storage facility

USA – United States of America

UTM - Universal Transverse Mercator

VNIR - Visible and near-infrared

1. Introduction

Raw materials from the mining and extractive industries are crucial for our daily lives. The global population is expected to increase to 8.5 billion by 2030, and the supply of raw materials for this increasing population is viewed as a global challenge. Specifically, the availability of raw materials is crucial for societal development. The demand for minerals is expected to double between 2010 and 2030 due to the green energy transition intended to meet the sustainable development goal (SDGs), as well as additional demands in the raw materials sector (European Union, 2016). As the demand for raw materials continue to increase, more resources must be mined to meet the increasing demand.

Globally, mining has been estimated to produce billions of tonnes of waste annually. This is expected to grow exponentially due to the increasing raw material demand and the extraction of minerals from ore deposits with lower grades. Mine waste is produced at different steps in the mineral process chain, including during: (a) mining, (b) mineral processing and metallurgy (classified as solid mining), and (c) processing of metallurgical wastes and mine waters. Mine tailing is but one component of processing and metallurgical waste. Tailings are known to be mixtures of crushed rock and processing fluids from mills, washeries or concentrators that remain after the extraction of economic metals, minerals, mineral fuels or coal from the mine (Lottermoser, 2010). When mining a metalliferous mineral resource, only a few percent of copper, zinc, lead or parts per million of gold are extracted (Lottermoser, 2010). This results in a small amount of valuable component being extracted and the production of large volumes of mine tailings. These mine tailings may contain minerals below the economic cut-off grade and are unfortunately lost due to processing inefficiency. These minerals, though non-economical when disposed as tailings, may become economical if there is an increase in market demand due to new applications and/or new and more efficient technologies to aid their recovery.

Mine tailings are stored in retaining dams known as tailing dams and range from benign to hazardous. Mine tailings are based on the mineralogy of the ore deposit from which they were produced from and the chemicals used in processing the ore such as cyanide. Mine tailings may pose safety, health and environmental risks. The main safety risk associated with active tailing dams, is dam failure due to: (a) meteorological conditions such as rainfall and snow melt, (b) poor monitoring, (c) poor site conditions, and (d) poor design/construction. Tailing dam failure has become well-known, as illustrated with the catastrophic failure of Vale's Corrego do Feijao mine in Brumadinho, Brazil in 2019. This particular event resulted in the release of 11.4 million m³ of mine waste into the environment, killing 259 people (Global Tailings Review, 2019). Furthermore, in their work, Rico *et al.* (2008) found that in Europe, out of the 26 cases of tailing dam failure compiled, 38% occurred in the UK and 56% were distributed between 9 other countries (Bulgaria, France, Ireland, Italy, Republic of Macedonia, Poland, Romania, Spain and Sweden). In addition to this, tailing dams pose environmental risks regardless of whether they are active or abandoned. These environmental risks include: (a) the generation of dust which can contain

a variety of hazardous substances such as radionuclides in the case of open tailing impoundment (Njinga *et al.*, 2017 cited in Nwaila *et al.*, 2021a); (b) heavy metal contamination; and (c) acid mine drainage (AMD). AMD results in the generation of acidic water, often characterized by a pH value <5 , caused by the oxidation of sulphide minerals by aerial exposure and/or the presence of oxygenated water (Taberima *et al.*, 2020). AMD has adverse effects on aquatic life and can mobilize heavy metals into surface and ground water systems (Taberima *et al.*, 2020).

The successful exploitation of mine tailings as a secondary resource (also known as an unconventional resource), akin to primary ore deposits, can be achieved when the tailings are characterized (Mulenshi *et al.*, 2021). In 2017, the European Commission reported in the Extractive Waste Directive (2006/21/EC) that the degree of valorisation is usually low, concluding there was a lack of strategic policies on mine waste valorisation (European Commission 2017a). Furthermore, it stated that of the reported 3,462 closed and abandoned mine waste facilities, 47 % were not specified in their resource characteristics.

Remote sensing has been used in the exploration of primary ore deposits over the past decades. Specifically, it has been applied in identifying spectral anomalies formed by ore deposit forming processes (Rajesh, 2004). Satellite remote sensing has been used for mineral mapping in mine tailings (Zabcic *et al.*, 2014, Kasmaeeyazdi *et al.*, 2021). Minerals and metals have special spectral characteristics that can be detected through remote sensing. The use of satellite remote sensing combined with machine learning (ML) can reduce time and cost for tailings storage facilities (TSF) mineral resource estimation and characterization.

Given the worldwide amount of existing mine waste, combined with the need to characterize them and their environmental footprint, in this research I propose the use of satellite remote sensing and machine learning for mineral resource estimation of defunct TSF owned by Sibanye-Stillwater in the Witwatersrand Basin in South Africa. In this research remote sensing data was combined with borehole drilling data to estimate the gold grade in the TSF. Gold grades were predicted using trained machine learning models and estimated for the borehole data using ordinary kriging (OK). Using tailings generated from the Witwatersrand goldfields as an example, this research proposes a novel methodology for mineral resource estimation in defunct TSF. The results of the research can be applied to tailing facilities in Europe given the similarities between the TSF construction and management in the Witwatersrand goldfields and Europe.

2. Aim and objectives

The aim of the research project is to explore the use of satellite remote sensing imagery with remote sensing for mineral resource estimation of the Lindum TSF (Witwatersrand Basin, South Africa). The expected outcome is the characterisation of the Lindum TSF and the generation of prediction maps using time series analysis.

To fulfil the aim, the following objectives will be addressed:

- Determine gold concentrations/grades in the TSF from satellite imagery.
- Develop prediction maps and models of the TSF using time series analysis.

2.1. Research questions

- Can satellite images acquired through Copernicus Satellite-2 be used to identify gold concentrations in a gold TSF?
- What are the most applicable image resolutions and band combinations for detecting gold concentrations in gold TSF?
- What are barriers and challenges to using satellite images in waste characterization and valorisation?
- What are the most suitable machine learning algorithm(s) for classifying satellite imagery for detecting gold concentrations?
- Are low resolution multispectral satellite images effective in determining gold concentrations in TSF?

3. Background

3.1. Industry collaborator

Sibanye-Stillwater Limited is an international mining and metals processing company whose portfolio includes metals processing and projects and investments. It has operations in the United States of America, South Africa, Canada and Finland. It was initially established in February 2013. The main commodities mined by the company are platinum, palladium, rhodium, and gold. It has become renowned internationally for its platinum group metals (PGM) catalytic platinum and palladium production being one of the world's leading producers.

3.2. Study area

The proposed study area is a TSF, located in the Witwatersrand Basin (Gauteng Province, South Africa), approximately 40 km west of Johannesburg, as shown in Figure 1. The TSF forms part of Sibanye-Stillwater's Randfontein surface gold and uranium operations. The TSF is a result of over 100 years of mining using inefficient mineral processing techniques. This resulted in some amounts of gold being disposed in the TSF. The TSF is subdivided into three sections or 'dumps', the Lindum Reefs no.1A which forms the base of the TSF, Lindum Reefs no. 2 and Lindum Reefs no. 1, which forms the top of the TSF (Figure 2). In 2007 and 2013 drilling programs along regularly spaced grids were conducted on the TSF as shown in Figure 3. Assay results for a borehole survey showed gold and uranium mineralization in the TSF, with varying grades for each section of the TSF. It was found that the gold mineralization was concentrated at the base of the main zone and it was proposed that the gold had migrated to this zone due to gravitational settling attributed to rainwater infiltration (Deswick Mining Consultants, 2014).

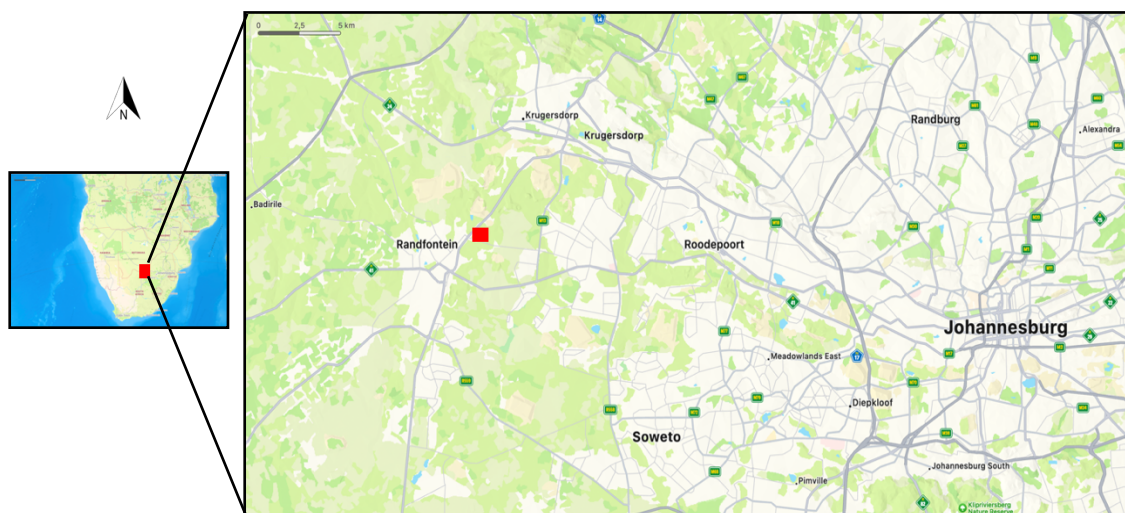


Figure 1. Location of the Lindum TSF in South Africa. The Lindum TSF is located at the red point.



Figure 2. Sections of Lindum TSF adapted from Deswick Mining Consultants (2014).



Figure 3. Borehole positions in sections of the TSF on top of LiDAR 3D geostatistical model.

3.2.1. Geological setting

The Mesoarchean Witwatersrand Supergroup is in the central north to north-eastern part of South Africa and is located in the centre of the Kaapvaal Craton. Its dimensions are at least 350 kilometres, in a north-easterly direction, and 200 kilometres in a north-westerly direction (Frimmel, 2014; Gold One International, 2013). The basin was formed over a period of 360 Ma between 3074 and 2714 Ma (Robb and Meyer, 1995). The Basin was formed when deltas were deposited by rivers flowing into an inland sea, depositing layers of sediments with a thickness of 7500 metres (Durand 2012). The Witwatersrand Supergroup shown in Figure 4 is divided into West Rand and Central Rand Groups. At the base of the Witwatersrand Supergroup are rocks of the West Rand Group which are overlain by rocks from the Central Rand Group (Agangi *et al.*, 2015). The West and Central Rand Groups are further subdivided. The West Rand Group consist of three units: (a) Hospital Subgroup, (b) the Government Subgroup, and (c) the Jeppestown Subgroup. The Central Rand Group is mineralised into the Subgroups, Johannesburg, which is said to contain the richest gold deposit mined and Turffontein (Durand, 2012). The Central Rand Super Group is the host to several gold-bearing 'reefs', most of which are concentrated in conglomerates (Robb and Meyer, 1995; Frimmel, 2005). The Ventersdorp Supergroup overlays the Witwatersrand Supergroup and consist of a base of gold bearing conglomerates that sits on the Central Rand Subgroup known as the Ventersdorp Contact Reef. The Ventersdorp Supergroup is covered by the Transvaal Supergroup and the younger Karoo Supergroup. The gold mined at the Randfontein operation occurs in quartz-pebble conglomeritic beds which are hosted in a thick succession of metamorphosed sediments (Gold One International Limited, 2013).

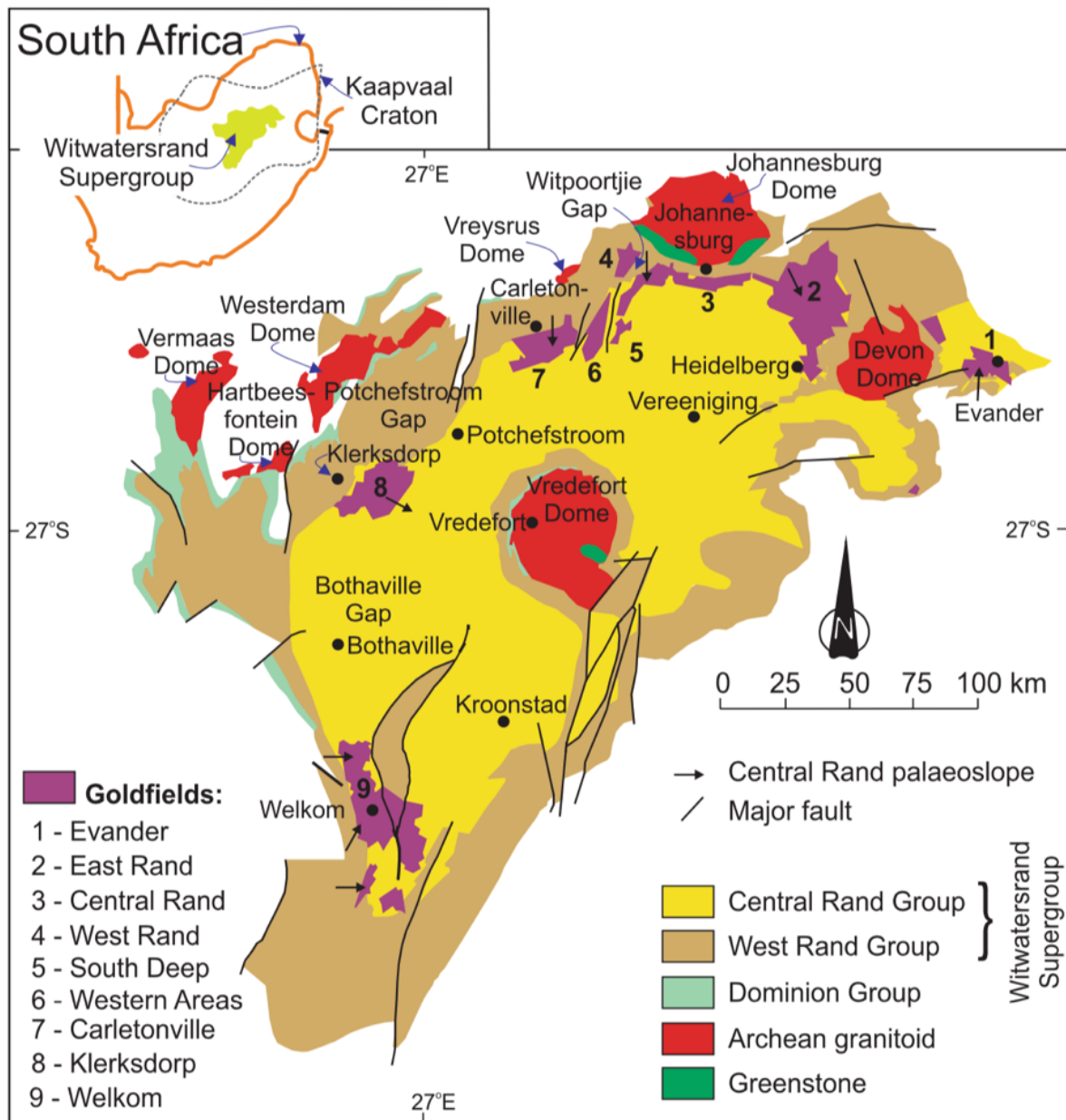


Figure 4. Regional geology map of Witwatersrand Basin and surrounding area (Modified after Frimmel, 2014).

3.3. Previous work

3.3.1 Valorisation of mine tailings

Valorisation refers to the economically viable utilization of a material stream which was once considered as non-valuable waste (Binnemans *et al.*, 2015). Waste valorisation aligns with the circular economy approach which aims to reduce the production of waste in the mining industry. This differs from the current mining industry's: take-make-waste approach. In works published by Kinnunen and Kaksonen (2019), and Parviainen *et al.*, (2020), the reason for valorisation of mine waste is linked to the world's need to meet sustainable development goals, as well as to reduce environmental and safety risks. Mine wastes stored in TSF are well known to pose environmental, health and safety risks. Additionally, maintenance costs for abandoned waste facilities are another key factor driving the need to valorise mine waste (Kinnunen and Kaksonen, 2019; Cavalho, 2016).

In the European Union (EU) there is an increasing interest in assessing the resource potential of anthropogenic resources to meet current mineral/metal demands (European Commission, 2011). Samples collected from bauxite and phosphogypsum (by-product of phosphate rocks) mine tailings both showed concentrations of rare earth elements (REEs). Examples include Mountain Pass (USA), having 3 to 5% rare earth oxide (REO) content, and Byan Obo (China) with 10% REE content, making them vast untapped resources for REEs (Binnemans *et al.*, 2015). As the demand of metals and minerals increases, waste valorisation could be a solution that solves two problems at the same time. Characterisation is a key step for the valorisation of mine waste. There are knowledge gaps in historical tailings characterisation, which must be filled (Mulenshi *et al.*, 2021; European Commission, 2018), including constructing resource estimation models to determine the economic feasibility of a mine tailing deposit (Blanning *et al.*, 2022; Kinnunen and Kaksonen, 2019).

3.3.2 Satellite remote sensing in mine waste valorisation and characterisation

Satellite remote sensing is the acquisition of data about an object on the earth surface without having physical contact with the object. Hyperspectral remote sensing has been used in the mining industry for ore deposit exploration by identifying and thematically mapping spectral anomalies of interest (Rajesh, 2004). Remote sensing can be an alternative to expensive TSF valorisation methods implemented by mining companies such as borehole drilling. Though remote sensing is a surface method, its use in mineral prospecting (Celik and Genc, 2021) is becoming invaluable. Remote sensing has been used to identify metal oxides and oxyhydroxides such as hematite, goethite and jarosite, as well as to predict tailings leachate pH in pyrite mine tailings (Zabcic *et al.*, 2014). Hunt (1977) demonstrated that numerous absorption bands exist for mineral structures due to elemental electronic transitions which are most often created by iron combined with water, hydroxyl ions or carbonates. Kasmaeeyazdi *et al.* (2021) used Sentinel-2 imagery to map aluminium in bauxite mining residues to address the lack of

sufficient in-situ samples for effective geostatistical modelling of material concentration variability. The method they employed confirmed the benefits of combining remote sensing and geostatistics for mapping metal variabilities. Further, Zhang *et al.* (2023a) highlighted the inadequacy of using traditional resource models and perspectivity maps which rely on static drill holes and sediment geochemical data for evaluating TSF. Their research suggested that transfer learning can be used to create dynamic resource models to evaluate large TSF without drilling additional boreholes and without additional geochemical data. Zhang *et al.* (2023b) demonstrated the use of machine learning and remote sensing to produce inferential models to generate accurate elemental maps by combining remote sensing data from Landsat-8 Operational Land Imager and Sentinel-2 satellites and geochemical data. As applications of remote sensing in mineral exploration are increasing, there are limitations to its use.

3.3.3 Machine Learning in mineral resource estimation

Mineral resource estimation is the determination of the grade and tonnage of a mineral deposit based on its geological and geochemical characteristics using various estimation methods (Dumakor-Dupey and Arya, 2021). Historically, geostatistics has been used for mineral resource estimations. Geostatistics is a branch of statistics, which entails the study of distribution in space applied to solve problems associated with ore deposit evaluation (Matheron, 1963). Geostatistics have been effective for estimating mineral resources of primary ore deposits. However, it performs poorly with extremely heterogeneous datasets, by over or under-estimating mineable resources, and requiring significant manual processing (Dumakor-Dupey and Arya, 2021). In addition to this, Nwaila *et al.*, (2020) argued that the standard industry practice for the evaluation of point-wise metal grades relies on assays which are costly and is typically limited for large ore bodies, thus introducing high degrees of uncertainties in their estimation. Even though highly accurate, a limitation of the approach is that it is not automatable, and the period between the initiation of the assay and the results was not negligible. As such they advocated for the adoption of ML resource estimation (Nwaila *et al.*, 2020).

ML is a sub-discipline of artificial intelligence based on a machine's ability to mimic biological learning (Mitchell, 1997, cited by Zhang *et al.*, 2023b; Zhang *et al.*, 2021c). There are numerous applications of ML in geoscience, including: (a) metal accounting (Ghorbani, Nwaila and Chirisa, 2022), (b) characterising objects and events, (c) estimating variables from observations, (d) long-term forecasting of geoscience variables, (e) mining relationships in geoscience data, and (f) target exploration (Zhang *et al.*, 2021a, 2021b). In addition to this, other useful applications of ML and data analytics are in processing legacy data for optimising metallurgical processes, as well as using legacy and operational data combined with automatable analytics to obtain data driven insights about mine process performance (Ghorbani *et al.*, 2020, 2021). Nwaila *et al.* (2020) demonstrated that machine learning-based predictive modelling methods, such as GS-Pred, is highly automatable, extensible and

produces results near-instantaneously, relative to assays, indicating that ML can be a viable tool for mine production, planning and target exploration.

ML algorithms classifies and predicts outcomes by learning the behaviour and patterns in training data (Lary, 2016; Dumakor-Dupey and Arya, 2021). ML algorithms can be supervised, unsupervised or semi-supervised, which is a combination of the two (Nwaila *et al.*, 2020; Zhang *et al.*, 2021c). The main difference between the two categories of ML algorithms is the labels in the training data subset (Berry *et al.*, 2019). In supervised machine learning, each sample consists of an input and a desired output and is used to analyse training data to generate a mathematical function used to map inputs to outputs (Zuo, 2017). In unsupervised machine learning, the algorithm recognises patterns without the involvement of a target attribute. That is, all the variables used in the analysis are used as inputs (Berry *et al.*, 2019). Supervised and unsupervised learning is further classified based on their capabilities, with supervised learning being classified as classification and regression algorithms (Berry *et al.*, 2019). Regression algorithms are continuous output algorithms that attempt to establish relationships between a predicted quantity and its features (Nwaila *et al.*, 2020). There are numerous ML algorithms used today for predictive modelling. The ML algorithms that belong to the supervised learning group are artificial neural networks (ANN), support vector machines (SVM), random forests (RF), logistic regression (LR) and the Bayesian network (Zuo, 2017). Autoencoder network, self-organizing map (SOM) and K-means clustering belong to the unsupervised learning group (Zou, 2017).

For this research, the details of all the unsupervised learning methods were not explored. Instead, more details on supervised learning methods that are used commonly in geoscience and more specifically in mineral resource exploration were explored. These algorithms are k-nearest neighbour (kNN), random forest (RF), adaptive boosting (AB) and extra trees (ET). The selection of the algorithms was based on factors highlighted by Zhang *et al.* (2021c) and includes, (a) computation time, (b) data density including feature space density, (c) bias-variance trade-off, (d) function complexity, (e) feature space dimensionality, (f) input and prediction and (g) feature interactions. These algorithms represent various potentially useful approaches that includes but is not limited to, a simple non-parametric approach (kNN), and ensemble and boosted approaches (RF and AB respectively) (Nwaila *et al.*, 2022). The kNN algorithm is a nonparametric simple instance-based learning algorithm (Kotsiantis *et al.*, 2007). Unlike other classifiers, it is not trained to produce a model (Maxwell *et al.*, 2018). The main principle of kNN during classification is that individual test samples are compared locally to k neighboring training samples in variable space, and their category is identified according to the classification of the nearest k neighbors (El Boucheffy and De Souza, 2020). The kNN locates the k-nearest instances to the query instance and determines its class by identifying the single most frequent class label (Kotsiantis *et al.*, 2007).

A RF classifier is an ensemble classifier that produces multiple decision trees, using a randomly selected subset of training samples and variables. This classifier has become popular within the remote sensing community due to the accuracy of its classifications (Belgiu and Drăguț, 2016). RF employs a

bagging operation and generates multiple decision trees based on randomly selected subset of the training data (Ge *et al.*, 2020). The majority ‘vote’ of all the trees is used to assign a final class for each unknown. This directly overcomes the problem that any one tree may not be optimal, but by incorporating many trees, a global optimum should be obtained (Maxwell *et al.*, 2018). One type of boosted decision tree which are also ensemble methods using decision tree is AB, or Adaboost. Decision trees are flowchart-like hierarchical structures that partition the trees recursively (Zhang *et al.*, 2021c). AB has three components: weak learners (the individual trees, which are individually poor predictors), a loss function that applies a penalty for incorrect classifications, and an additive model that allows the individual weak learners to be combined so that the loss function is minimized (Maxwell *et al.*, 2018). In ET, a group of unpruned decision tree is created in accordance with the traditional top-down method and involves randomizing both attribute and cut-point selection while splitting a node of a tree (Ampomah, Qin and Nyame, 2020). Like RF, ET is a tree-based ensemble method and is proposed as computationally efficient and highly randomized extension of RF (John *et al.*, 2016). The two differs in that, unlike RF, ET does not use bagging to generate the training subset to develop trees and ET randomly selects the best feature to split the node in the node-splitting step (John *et al.*, 2016).

4. Data and Methods

4.1. Source of data

The remote sensing data used for this research was acquired from the Copernicus programme's Sentinel-2 satellites. The objective of the Copernicus programme is to continuously gather high resolution optical images over land and coastal regions (Ge *et al.*, 2018). The programme was developed by the European Commission. Sentinel-2A and 2B, are satellites in the family of Sentinels in the Copernicus programme. The satellites were specifically developed by the European Space Agency (ESA) to complement remote sensing services for vegetation, land cover and environmental monitoring (U.S. Geological Survey, 2018). The Sentinels have multispectral cameras and are designed as twins of satellites to reduce their revisit times, hence reducing the image acquisition time (U.S. Geological Survey, 2018). Sentinel-2 was the second twins launched in the Copernicus program. Sentinel-2A was launched on 23 June 2015 at 01:52 UTC from the ESA's base in French Guiana and Sentinel-2B was launched on the 7 March 2017 at 01:49 UTC.

Sentinel-2 collects data between north latitude 83 degrees and 56 latitudes south. Sentinel-2 carries a multispectral instrument (MSI) which can measure 13 bands (B1 to B12) in the visible and near-infrared (VNIR) to shortwave infrared (SWIR) wavelengths along a 290 kilometres orbital swath at different spatial resolutions (U.S. Geological Survey, 2018; European Space Agency, 2022). Each band has its own characteristics as shown in Table 1 and measure electromagnetic (EM) wave reflectance along various points of the EM spectrum. The spatial resolution of the 13 bands ranges from 10 to 60 metres with bands 1, 9 and 10 having a spatial resolution of 60 metres; bands 2, 3, 4 and 8 with spatial resolution 10 metres and bands 5, 6, 7 and 8A having spatial resolution 20 metres Table 1. Bands 1 to 12 were used for this research. However, bands 1, 9 and 10, were not used in data processing due to Sentinel band 10 being uncalibrated. This results in noise patterns on bright images caused by detector saturation (Ge *et al.*, 2020). Bands 1 and 9 were used for atmospheric correction.

The estimated revisit time is 10 days for Sentinel-2 with 5 days for each Sentinel-2 satellite. The Sentinel-2 image acquired were from the 24 August 2015 to 4 October 2019 (Table 2). The metadata information for the first image of the series is: "coordinate reference system (CRS) from European Petroleum Survey Group (EPSG) 32735, Transform: Affine [20, 0, 499980, 0, -20, 7200040]; ID: COPENICUS/S2/20150824T082656_20150824T082659_T35JNM; Version: 1618001523716097; Data taken identifier: GS2A_20150824T082656_000890_N02.04; 'SPACECRAFT_NAME': 'Sentinel-2A'". Bands 1 to 12. Sentinel-2 MSI products are fixed size granules or tiles. These granules consist of 100 x 100 kilometer squared ortho-images in Universal Transform Mercator (UTM)/WGS84 projection, with one tile per spectral band (European Space Agency 2015). The L1C-level Sentinel granules were used for this research. The images used the UTM coordinate projection and the World Geodetic System 1984 (WGS84) datum.

Geochemical data in the form of gold assays was acquired from the company, Sibanye-Stillwater. The data was acquired in 2013 during the company's drilling program to determine the reclamation potential of the Lindum TSF. The gold assays were taken from boreholes along an equally spaced 10 x 10 metres grid. The coordinates of the boreholes were adjusted for confidentiality for the purpose of this research. All the coordinates were converted to UTM geographical coordinate system and WGS 84 datum to confirm with the coordinates system of the satellite images. The data contained in the gold assay dataset included, x and y coordinates, gold grade in grams per tonnes (g/t), borehole depth and borehole spacing.

Table 1. Sentinel-2 satellite image band characteristics. (Available online: <https://sentinels.copernicus.eu/web/sentinel/missions/sentinel-2/instrument-payload/resolution-and-swath>).

| VNIR | Bands | Description | Sentinel-2A | | Sentinel-2B | | Spatial resolution (m) |
|------|-------|---------------------|-------------------------|----------------|-------------------------|----------------|------------------------|
| | | | Central wavelength (nm) | Bandwidth (nm) | Central wavelength (nm) | Bandwidth (nm) | |
| VNIR | B1 | Aerosol | 442.7 | 21 | 442.2 | 21 | 60 |
| VNIR | B2 | Blue | 492.4 | 66 | 492.1 | 66 | 10 |
| VNIR | B3 | Green | 559.8 | 36 | 559.0 | 36 | 10 |
| VNIR | B4 | Red | 664.6 | 31 | 664.9 | 31 | 10 |
| VNIR | B5 | Vegetation red edge | 704.1 | 15 | 703.8 | 16 | 20 |
| VNIR | B6 | Vegetation red edge | 740.5 | 15 | 739.1 | 15 | 20 |
| VNIR | B7 | Vegetation red edge | 782.8 | 20 | 779.7 | 20 | 20 |
| VNIR | B8 | NIR | 832.8 | 106 | 832.9 | 106 | 10 |
| VNIR | B8A | NIR | 864.7 | 21 | 864.0 | 22 | 20 |
| VNIR | B9 | Water vapour | 945.1 | 20 | 943.2 | 21 | 60 |
| SWIR | B10 | Cirrus | 1373.5 | 31 | 1376.9 | 30 | 60 |
| SWIR | B11 | SWIR | 1613.7 | 91 | 1610.4 | 94 | 20 |
| SWIR | B12 | SWIR | 2202.4 | 175 | 2185.7 | 185 | 20 |

Table 2. Sentinel-2 images and the date of acquisition. Images acquired from 24 August 2015 to 04 October 2019.

| | Remote Sensing file name |
|-----------|--|
| 0 | COPERNICUS_S2_20150824T082656_20150824T082659_T35JNM.tif |
| 1 | COPERNICUS_S2_20151003T075826_20151003T082014_T35JNM.tif |
| 2 | COPERNICUS_S2_20160207T075102_20160207T081608_T35JNM.tif |
| 3 | COPERNICUS_S2_20160430T080012_20160430T082712_T35JNM.tif |
| 4 | COPERNICUS_S2_20160706T074942_20160706T081431_T35JNM.tif |
| 5 | COPERNICUS_S2_20161007T080002_20161007T082247_T35JNM.tif |
| 6 | COPERNICUS_S2_20170316T075651_20170316T081607_T35JNM.tif |
| 7 | COPERNICUS_S2_20170402T074931_20170402T081156_T35JNM.tif |
| 8 | COPERNICUS_S2_20170706T074609_20170706T080902_T35JNM.tif |
| 9 | COPERNICUS_S2_20171004T074919_20171004T081651_T35JNM.tif |
| 10 | COPERNICUS_S2_20180303T074819_20180303T081305_T35JNM.tif |
| 11 | COPERNICUS_S2_20180407T074611_20180407T081314_T35JNM.tif |
| 12 | COPERNICUS_S2_20181007T075811_20181007T081838_T35JNM.tif |
| 13 | COPERNICUS_S2_20190122T075221_20190122T081410_T35JNM.tif |
| 14 | COPERNICUS_S2_20190427T074619_20190427T081452_T35JNM.tif |
| 15 | COPERNICUS_S2_20190701T074621_20190701T080914_T35JNM.tif |
| 16 | COPERNICUS_S2_20191004T074749_20191004T080733_T35JNM.tif |

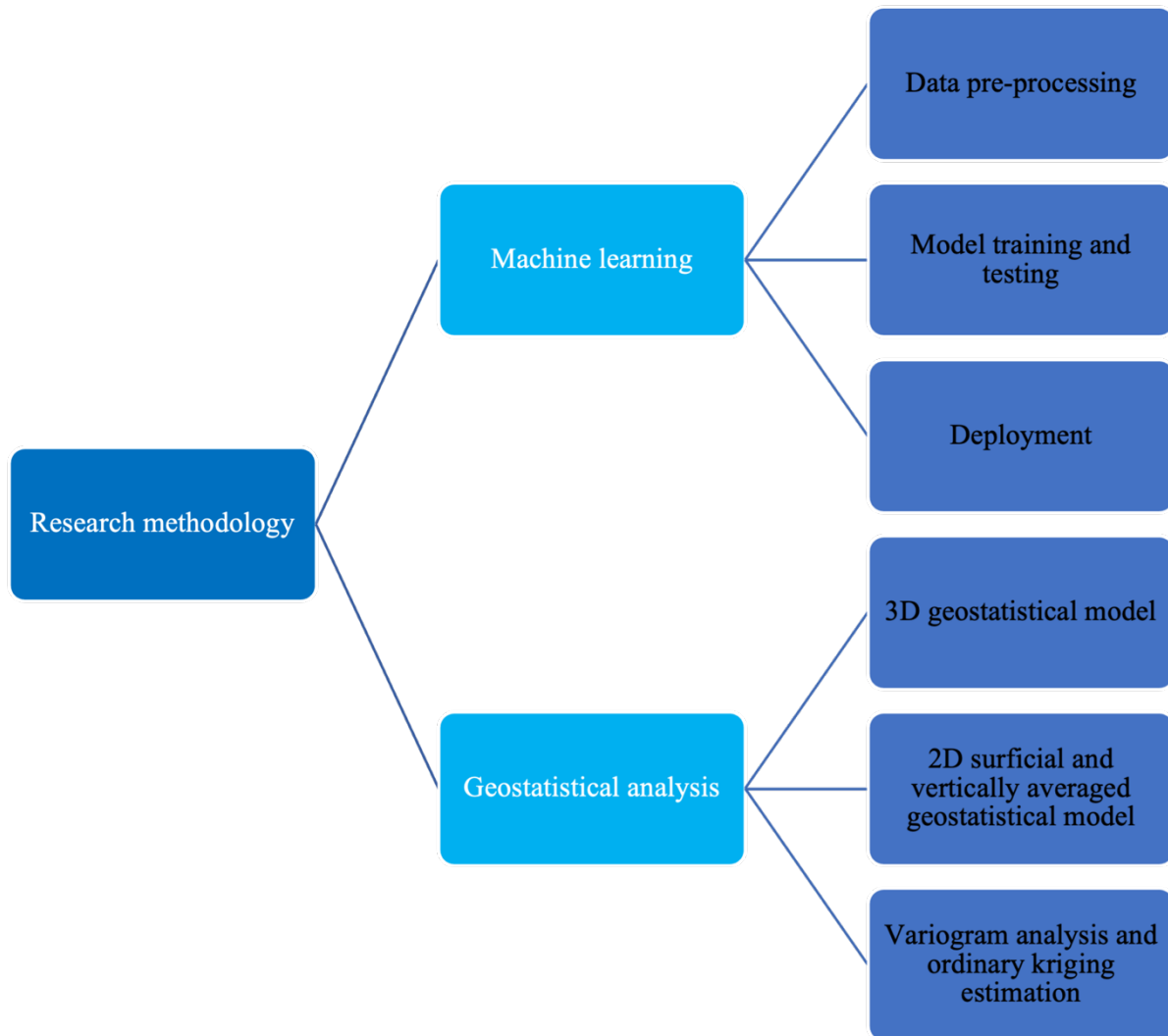


Figure 5. Block diagram of the research methodology.

4.2. Geostatistical based predictive modelling

The steps followed for geostatistical based predictive modelling are displayed in Figure 5. Predictive modeling is the process of developing a mathematical tool or model that generates an accurate prediction (Kuhn and Johnson, 2013). Predictive modelling is used in various disciplines such as geoscience, biomedical science, finance, and gaming. Predictive modelling has been used in geoscience since the 1960s in France by Matheron who developed Kriging after the name of Daniel G Krige. He was probably the first to make use of spatial correlation and best linear unbiased estimator in the field of mineral resource evaluation (David, 2012). Kriging can be defined as a progressive interpolation method for the estimation of a regionalized variable at selected points (Krige, 1951; Matheron, 1963; Nwaila *et al.*, 2020).

4.2.1. 3D Block model

Geostatistical predictive modelling was used in this research to develop a three-dimensional geostatistical model using borehole data acquired from Sibanye-Stillwater. The borehole data was used to develop the three-dimensional (3D) geostatistical resource model using Ordinary Kriging (OK) estimation (Figure 6). To develop the 3D block model, an exploratory data analysis was done before processing the data. Descriptive statistics of the dataset and the probability distribution function for the data was plotted using a histogram as displayed in Chapter 5. In addition, this step was done to detect and remove outliers and ensure data accuracy for the geographic coordinates and gold assay values. OK estimator was used to estimate the gold grades at unsampled locations within the TSF. Two key conditions for OK are, a Gaussian or normally distributed dataset and the spatial covariances. Data is normally distributed normally when it has a mean of zero or has the probability distribution of a bell-shaped curve. A normal-score transformation was done on the data to ensure the data was normally distributed for the Kriging estimation.

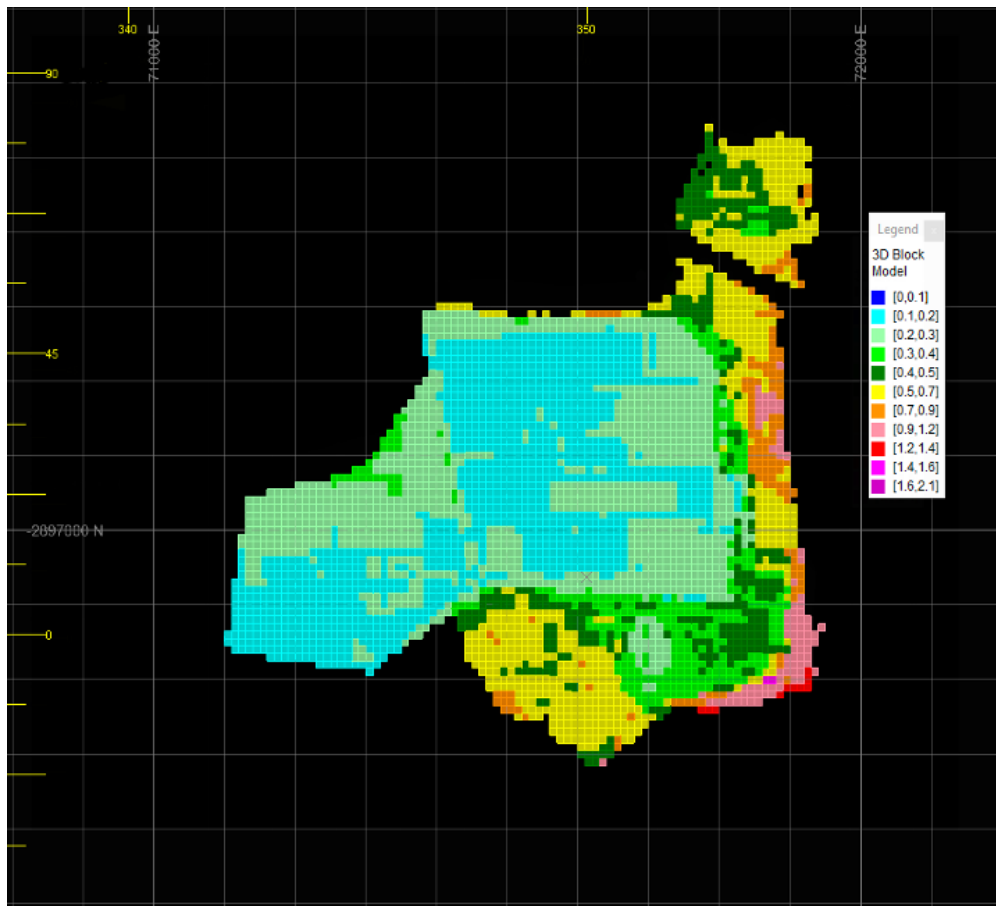


Figure 6. 3D geostatistical block model of the TSF.

4.2.2. Variogram analysis

Variogram models and anisotropic ellipsoid are commonly used for spatial interpolation (Zerzour *et al.*, 2021) and is a preliminary step in the Kriging estimation (Lamamra *et al.*, 2019). The underlying assumption of Kriging is that a random field yield results that are better correlated when the distance between the observations is smaller and the direction of the observation is favorable (Nwaila *et al.*, 2020). Kriging utilizes the variogram, which does not depend on the actual value of the variable (data), rather its spatial distribution and internal spatial structure (Akbar, 2012). As a result of this, to calculate the Kriging weights and estimation, a variogram analysis was done to determine the global variances in the TSF. The experimental variogram was calculated using equation 1.

$$\gamma(h) = \frac{1}{2N(h)} \sum_i^{N(h)} [(Z(x_i) - Z(x_i + h))^2] \quad \text{Equation 1}$$

$\gamma(h)$ is the experimental variogram obtained from data values.

x_i : location of the sample.

$Z(x_i)$: the values of the sample.

$N(h)$: the number of the pairs $(x_i, x_i + h)$ separated by a distance h .

$Z(x_i + h)$ is a value at location $x_i + h$.

In Ordinary Kriging the sum of the weights is constrained to equal to 1. This allows for building a Kriging estimator that does not require prior knowledge of the stationary mean, yet remains unbiased in the sense (Akbar, 2012). The Kriging estimator is represented by equation 2 and the estimation error in equation 3.

$$\hat{Z}(x_0) = \sum_{i=1}^n \lambda_i Z(x_i) \quad \text{Equation 2}$$

Where $\hat{Z}(x_0)$ is the Kriging estimate at location x_0 ; $Z(x_i)$ the sampled value at location x_i and λ_i the weighting factor for $Z(x_i)$. The estimation error is:

$$\hat{Z}(x_0) - Z(x_0) = R(x_0) = \sum_{i=1}^n \lambda_i Z(x_i) - Z(x_0) \quad \text{Equation 3}$$

where $Z(x_0)$ is the unknown true value at x_0 ; and $R(x_0)$ the estimation error. For an unbiased estimator, the mean of the estimation error must equal zero.

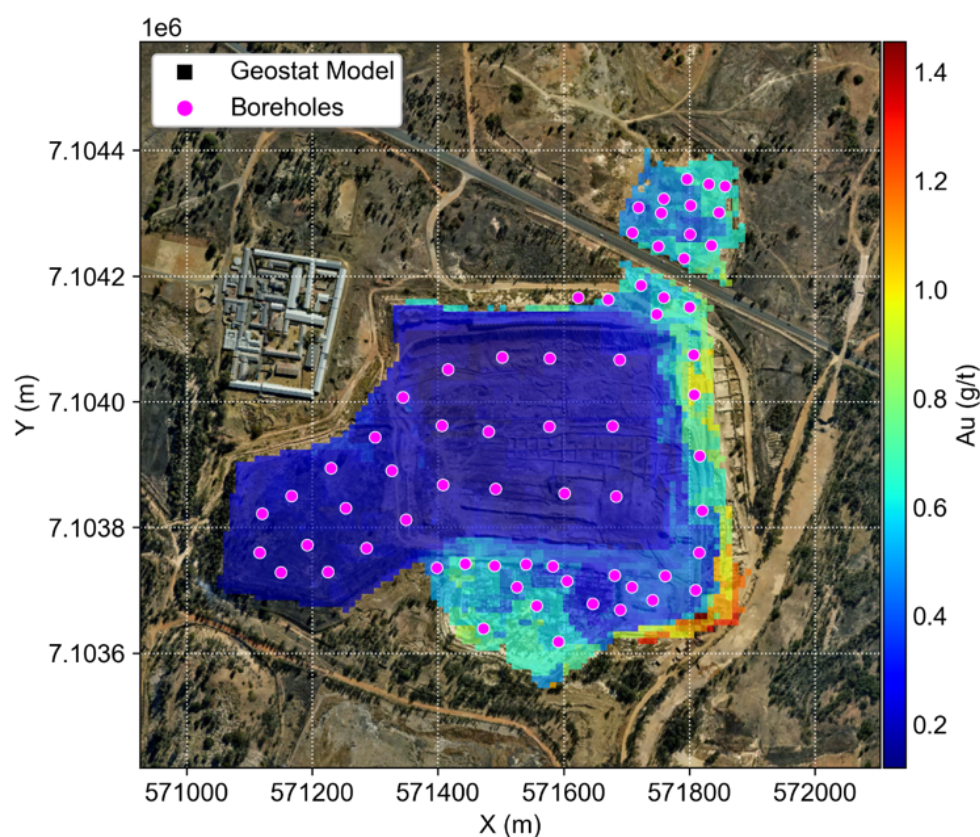
$$E \{R(x_0)\} = 0. \quad \text{Equation 4}$$

and

$$\sum_{i=1}^n \lambda_i = 1 \quad \text{Equation 5}$$

4.2.3. 2D surficial and 2D vertically averaged geostatistical models

A tabular surficial two-dimensional (2D) geostatistical model was developed from the 3D geostatistical model following the methodology of Zhang *et al.* (2023b) using data points located close to the surface of the TSF at a maximum depth of 5 metres (Figure 7). Like the 3D geostatistical model, this surficial model is also a static model. As such it is unable to capture vertical changes in the TSF derived over time due to water infiltration and internal slumping (Deswick Mining Consultants, 2014). This was done to ensure the most accurate comparison of the geostatistical model and the prediction maps developed using ML models.



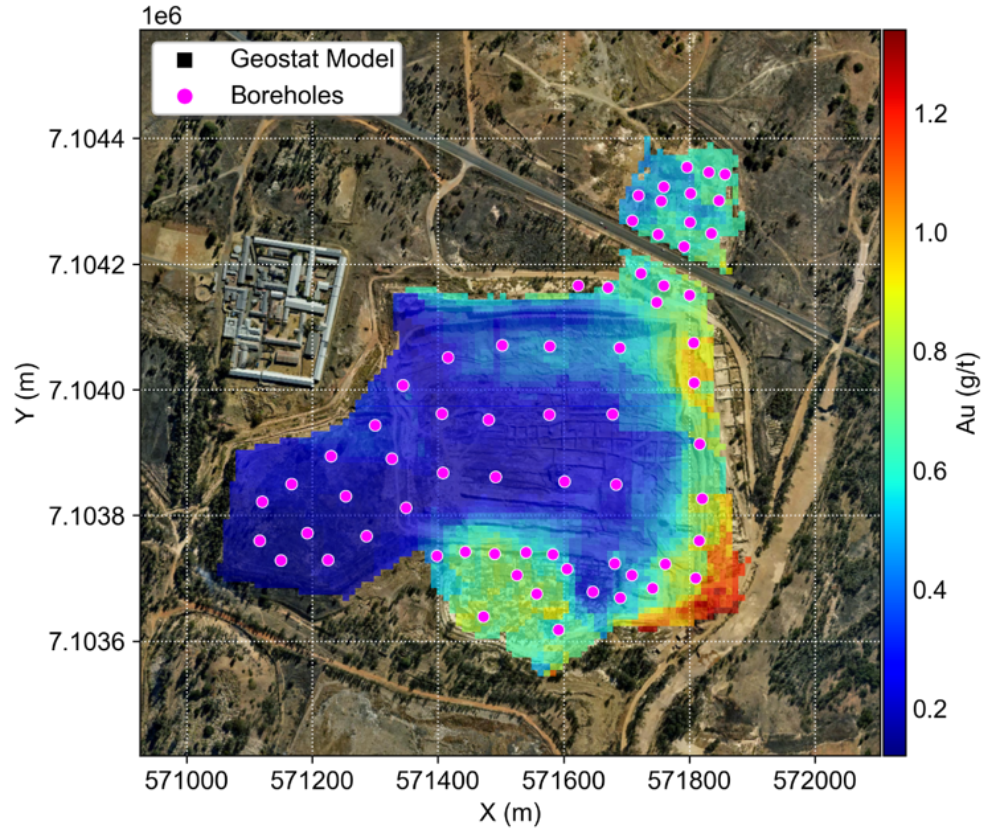


Figure 7. Visualization of 2D vertically averaged (a) surficial (b) geostatistical model of the of the TSF, using ML overlaid on top of the satellite-borne imagery of the TSF (Zhang *et al.*, 2022a).

4.3. Machine learning-based predictive modelling

Machine learning (ML) is a sub-discipline of artificial intelligence used to model and predict patterns in large and/or complex datasets. The workflow in supervised machine learning algorithm deployment presented by Nwaila *et al.* (2020) was used for the supervised classification in this research. This includes: 1) data pre-processing; 2) classification/regressor training; 3) tuning of hyperparameters; and 4) performance evaluation (Figure 8).

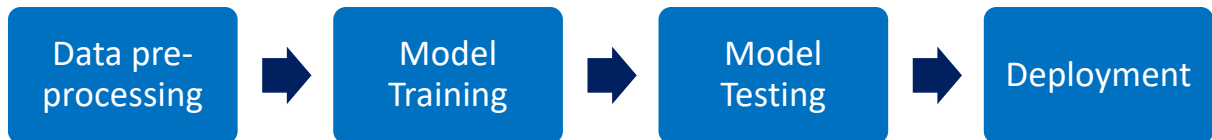


Figure 8. ML methodology followed the steps outlined in the block diagram. Adapted from Nwaila *et al.*, 2020.

4.3.1. Data pre-processing

The satellite images were treated initially in a pre-processing step to ensure data quality and to reduce errors during processing. In the pre-processing step, actions taken were: 1) atmospheric correction models were applied to remove the effects of the atmosphere, 2) radiometric calibration, 3) geometric correction, and 4) noise removal (Nwaila *et al.*, 2022). The satellite images used in this research consisted top of the atmosphere (TOA) reflectance, as such, they contained contributions from the atmosphere. The presence of small and large particles in the atmosphere can cause absorption, refraction and scattering of electromagnetic (EM) waves reflected from surfaces on the earth surface and transmitted to satellite sensors. This can affect quantitative analysis during image processing as they can introduce errors into the process.

Atmospheric correction involved the estimation of atmospheric parameters and the retrieval of surface reflectance (Liang and Wang, 2019). It was used to remove the presence of scattered or reflected waves due to gases and aerosols present in the atmosphere on the reflected waves measured by the MSI. The Fast Line-of-Sight Atmospheric Analysis of Spectral Hypercubes (FLAASH) method was used for atmospheric correction. This method is based on first-principles atmospheric correction and corrects wavelengths up to 3 metres in the VNIR, and SWIR ranges (Nwaila *et al.*, 2022). Noise interfering with an image system can affect final display effect of the image. This is derived from the photoelectric detectors and can take the form of dark current noise, thermal noise and photon shot noise (Zheng and Xu, 2021). Removal of these noise effects can increase image value as it increases the image quality.

Geometric correction, also known as georeferencing was done in the pre-processing step. It was used to ensure that all datasets used in the processing step were in the same geometric coordinate system. In this case, the coordinate system of the images was transformed to UTM along with the gold assay borehole data. Satellite sensors collect data along a path and as the satellites move the angle of reflectance changes giving rise to variation of light on images which can affect image interpretation and classification (Government of Canada, 2015). Radiometric calibration removes these inferences and increases the quality of the image.

4.3.2. Model training

Model training followed the method used by Zhang *et al.* (2023b). Training data was acquired from Dump 20, a TSF located 3 kilometres north of the Lindum TSF for which geochemical data was available in the form of a high-resolution 3D model (Figure 9). The geochemical data and satellite images from Landsat-8 Operational Land Imager and Sentinel-2 were first fused together. Satellite images for the two satellites were used because the images acquired from the Sentinel-2 satellite had missing data due to anthropogenic disturbance in the TSF when the images were acquired. The images from the Landsat-8 satellite were used to provide the missing data. As such when the images from Sentinel-2 were processed, this section of the TSF was removed and replaced with the data from

Landsat-8 to ensure an accurate representation of the TSF. It is common practice in ML to separate the dataset into three groups, one part for use as training data, another for testing and the last for model validation, in the method called train/test split (Boroh *et al.*, 2022). The dataset was segregated using this method and the parameter grid defined. The parameters for the models can be found in Table 3 (see Appendix C) and is based on Nwaila *et al.* (2022). The Geostatistical Software Library (GSLIB) (Deutsch, 1992) was used for model training and data processing. This software ran on the Python 3.10.6 language for the data processing step.



Figure 9. Satellite image of Dump 20 TSF where training data was obtained from and Lindum TSF (Zhang *et al.*, 2023a).

Dimensionality reduction was performed on the 3D model to produce a 2D model which was later fused with the satellite images. This was to ensure accurate fusing of the images acquired using satellite remote sensing which is a 2D surface method. The surface data points of the 3D model located at 0 – 10 centimetres below the surface were used to acquire geochemical data for the surface of the TSF. The 3D model was made up of 276, 622 gridded points at a resolution of 0.5 metres with variable volumetric coverage (Zhang *et al.*, 2023b). The 2D surface model consisted of 63.65% of the total data points of the 3D model. The geometric coordinates of the 2D surficial model were then matched with the Landsat-8 satellite images using a grid search using the Spearman rank correlation, averaged across all bands (Zhang *et al.*, 2023b). This was to ensure accurate match of the coordinates and the data with the time when the geochemical data was acquired with the satellite images.

Table 3. Parameter grid for employed machine learning algorithms.

| Method | Parameters | Model Name |
|--------|---|------------|
| kNN | number of neighbours = 3 | Au_kNN |
| RF | max depth = 25, max features = 8, min samples per leaf = 1, min samples per split = 6, number of estimators = 1500 | Au_RF |
| ET | max depth = 27, max features = 9, min samples per leaf = 1, min samples per split = 2, number of estimators = 1000 | Au_ET |
| AB | base estimator = decision tree, base estimator max depth = 26, base estimator max features = 6, base estimator min samples per leaf = 2, base estimator min samples per split = 3, number of estimators = 500 | Au_AB |

4.3.3. Model cross-validation

To evaluate each model to determine the robustness of the models generated, validation tests are carried out to determine model performance by comparison of the actual data with the estimated data. Three methods are used for model validation for geostatistical and ML prediction models (A.W. Boroh *et al.* 2022). The three methods are the coefficient of determination (CoD) or R^2 , the mean absolute error (MAE) and the root mean square error (RMSE) (A.W. Boroh *et al.*, 2022). For this research, two of the validation methods were used to validate the ML models and measure the performance of the geostatistical estimations. The CoD ranges from 0 to 1 and is a measure that shows how the difference in one variable usually a dependent variable can be used to show the difference in another variable. The closer the CoD to 1, the better the model. The function that depicts this is shown in equation 6.

$$R^2 = 1 - \frac{\sum_{i=1}^n (y_i - \hat{y}_i)^2}{\sum_{i=1}^n (y_i - \bar{y})^2} \quad \text{Equation 6}$$

The MAE is depicted in equation 7. MAE is a measure of the actual values and the predicted values. It is also referred to the measure of residuals.

$$MAE = \sqrt{\frac{1}{n} \sum_{i=1}^n (y_i - \hat{y}_i)^2} \quad \text{Equation 7}$$

4.3.4. Deployment

The deployment area was the Lindum TSF in the Witwatersrand goldfields of South Africa. The remote sensing images cover an area of 1.12 squared kilometres.

5. Results

This chapter presents the results of the research based on the methodologies described in Chapter 4. The results are discussed in the context of previous work in the literature reviewed.

5.1. Integration of geostatistical and machine learning models

Qualitative and quantitative comparisons were made between the 2D geostatistical models, and the prediction maps generated from the four ML models described in Chapter 3. The Sentinel-2 image, 24 August 2015 was used for the comparison between the 2D surficial geostatistical model, and the prediction maps generated using the ML models (Figure 10). The satellite image acquired closest to the time when the borehole survey was carried out on the TSF in 2013 was used in the comparison. This ensured the best comparison between ML and geostatistical methods. A visualization of the prediction maps generated by the four ML models shows high-grade gold pixel clusters in Section 1A of the TSF located north of the R41 road (Figure 10). This high-grade gold pixel cluster is prominent in the prediction map generated by the kNN model but is not observable in the 2D geostatistical models. In contrast, the 2D geostatistical models shows clusters of high-grade gold pixels in Section 1A located in the south-eastern section of the TSF. This is absent in all the prediction maps shown in Figure 10.

Medium to high-grade gold pixel cluster is evident in Section 1A in the southern section of the of the TSF in all the prediction maps while lower grade pixel cluster can be seen in the 2D geostatistical models. Medium-grade gold pixel cluster is evident in prediction maps generated by AB, RF and kNN models in the Section 1 of the TSF located south of the main road and trending west to east. This cluster is not observable in the 2D geostatistical models for which lower gold grades are depicted. This confirms to the work of Boroh *et al.* (2022). They compared geostatistical and machine learning models for predicting geochemical concentration of iron and found that ML techniques such as kNN and RF performed better than geostatistical methods such as OK.

The mean gold grade predicted by the ML models is 0.44 g/t (Table 4). In comparison with the ML models, the mean gold grade was the same when rounded to three decimal places for the 2D vertically averaged model, but lower for the 2D surficial geostatistical model. The predicted gold grade were 0.35 g/t and 0.44 g/t for the 2D surficial geostatistical model and the 2D vertically averaged geostatistical model respectively. This difference in mean gold grades can be attributed to the fact that the surficial 2D geostatistical model was developed using surficial data points, while the vertically averaged 2D model captured greater depths of tailing in the TSF. In addition to this, the number of samples used for the predictions was higher for the ML models, with each having a sample count of 4048. The 2D geostatistical models had fewer samples, with each having a sample count of 3819.

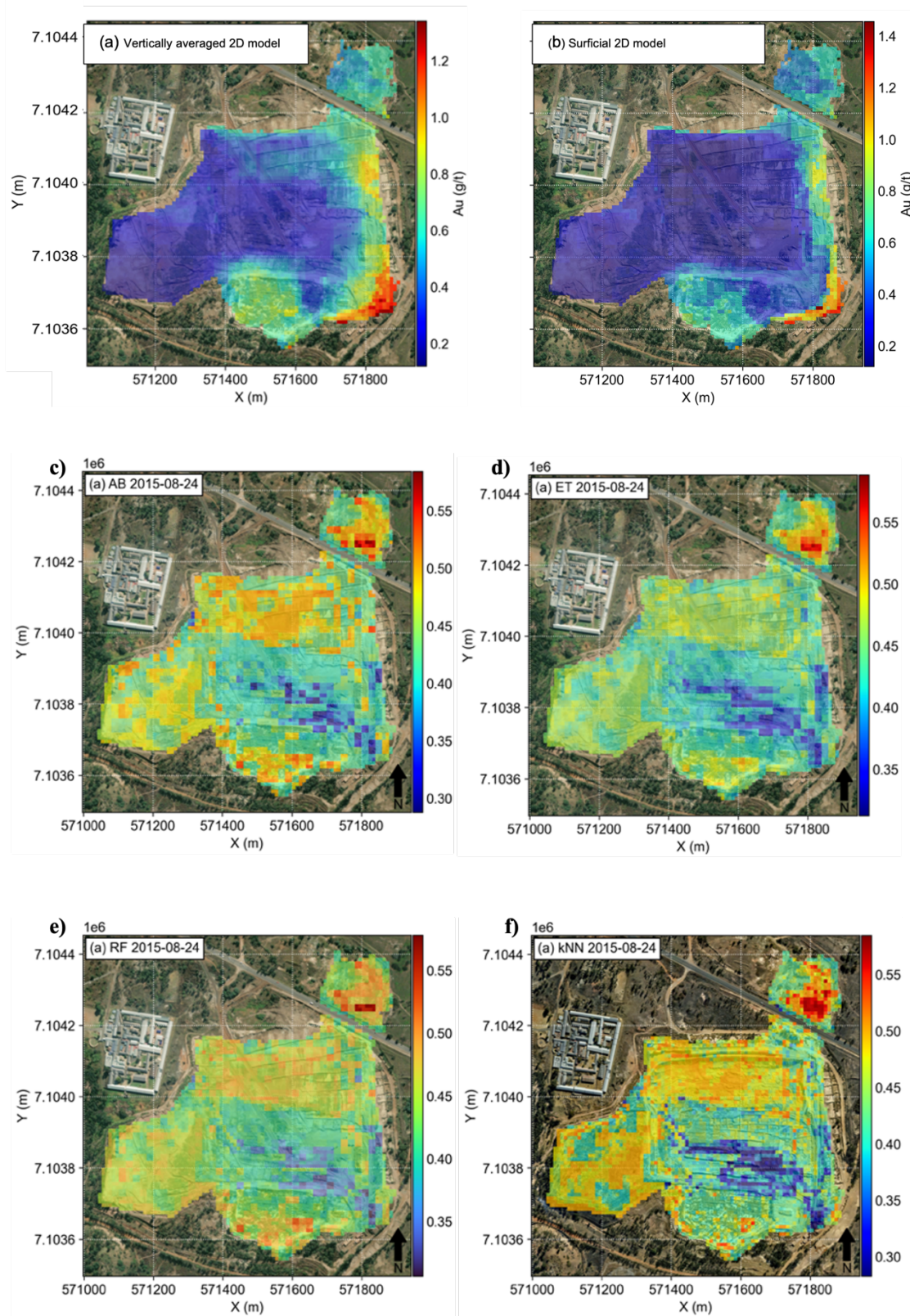


Figure 10. (a, b) 2D geostatistical models; ML models using the image taken on 2015-08-24. (c) Abo boosting, (d) extra trees (I, (e) random forest (RF), (f) K-nearest neighbor (kNN). Visual differences between prediction maps *the* from ML models and *the* geostatistical models.

Table 4. Descriptive statistics of the predicted gold grades.

| Resource model type | Count of samples | Gold grade STD (g/t) | Gold grade mean (g/t) |
|---|------------------|----------------------|-----------------------|
| 2D surficial geostatistical model | 3819 | 0.22 | 0.35 |
| 2D vertically averaged geostatistical model | 3819 | 0.23 | 0.44 |
| kNN | 4048 | 0.04 | 0.44 |
| RF | 4048 | 0.03 | 0.44 |
| ET | 4048 | 0.03 | 0.44 |
| AB | 4048 | 0.04 | 0.44 |

A histogram plot comparing the predicted gold grades using the four ML models and the geostatistical models was plotted (Figure 11). This plot illustrates the distribution of the predicted gold grades for the ML models and the 2D geostatistical models. The mean predicted gold grades was observed to be higher for the ML models and the standard deviations were lower compared to the 2D geostatistical models. The wide spread of gold grades in the histogram plots for the 2D geostatistical models corresponds to the high standard deviations observed.

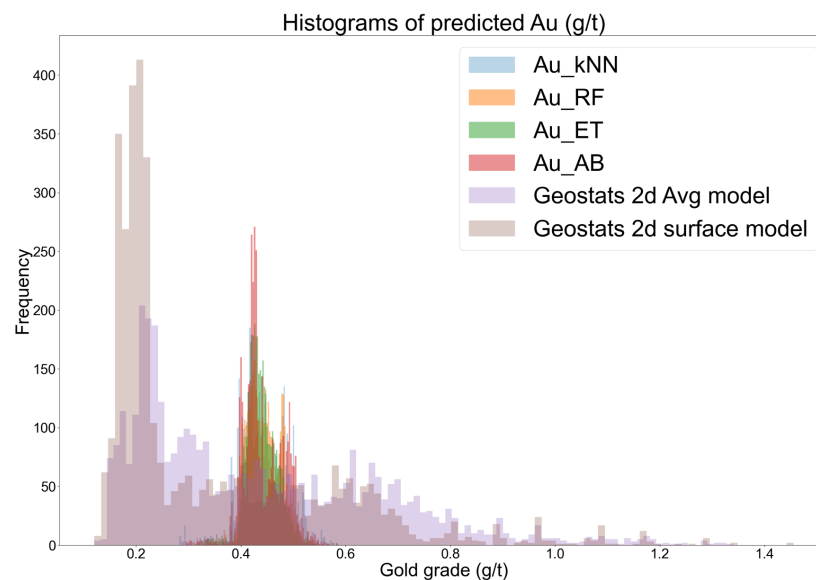


Figure 11. Histogram of predicted gold grades for the 2D geostatistical and ML models. The geostatistical model histograms show bimodal behavior.

5.2. Transfer of machine learning models for predictive block modelling

The performance of the machine learning models for the training and testing datasets was evaluated using the CoD value. The CoD value indicates the total variation in the predictions made by the models, as given in the predicted gold grades and those estimated using OK (Celik and Genc, 2021). The results showed AB, RF and ET models were the best performers for predicting gold in the TSF, compared to the kNN model. The CoD values for the ML predictions were 0.95 for AB, 0.92 for ET, 0.87 for RF, and 0.70 for kNN. This indicates that all machine learning models performed well at predicting gold in the TSF. A scatter plot comparing the actual gold grades predicted using the ML models and the OK gold estimates showed that the RF and ET plots had closer clusters of data points around the regression line, while the AB and kNN plots were more scattered (Figure 12). The CoD values were 0.62 for AB, 0.75 for ET, 0.66 for RF, and 0.59 for kNN (Table 5). This shows a decrease in the CoD values when OK is performed on the predicted gold values. It should be noted that as OK was performed on the predicted gold grade values, all model performance decreased, with AB showing the highest decrease at 33 %, and kNN showing the lowest at 11 %.

Further, a visual observation of the OK estimation maps (Figure 13) shows the differences in the spatial distribution of the gold grades on the surface of the TSF. This shows that OK estimations were visually similar to the actual gold grades predicted by the ML models. In the AB and RF estimation maps, similar patterns of high gold grade estimates can be seen (Figure 13). This is also observed for ET and kNN but are less prominent.

Table 5. Comparison of CoD for the ML model prediction and the Kriged prediction values.

| | AB | ET | RF | kNN |
|--------------------------------|-----------|-----------|-----------|------------|
| R² ML Models | 0.95 | 0.92 | 0.87 | 0.70 |
| R² ML Kriged | 0.62 | 0.75 | 0.66 | 0.59 |
| Reduction factor (%) | 33 | 17 | 21 | 11 |

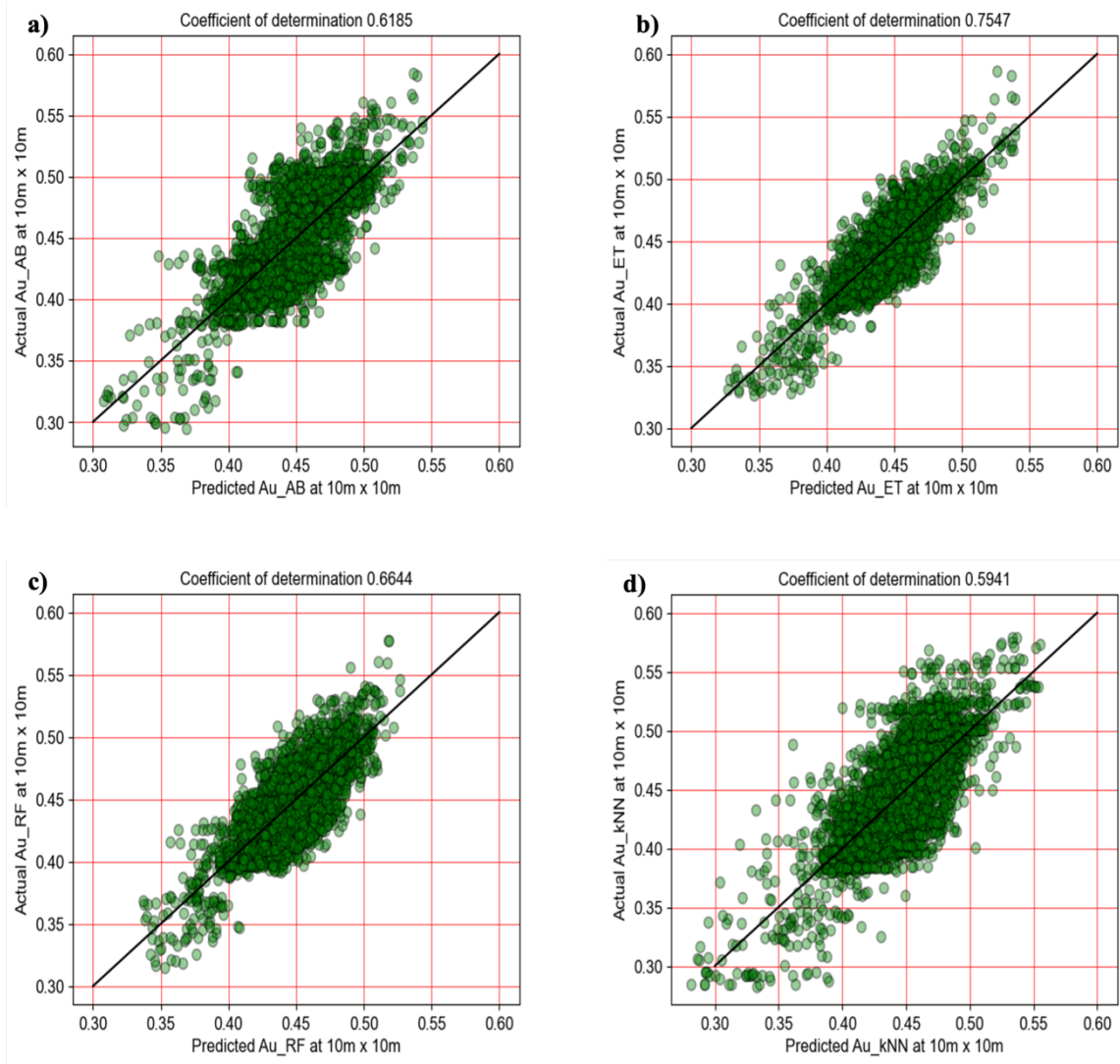


Figure 12. CoD plot of ML methods for gold grade prediction in the TSF. (a) AB, (b) ET, (c) RF and (d) kNN.

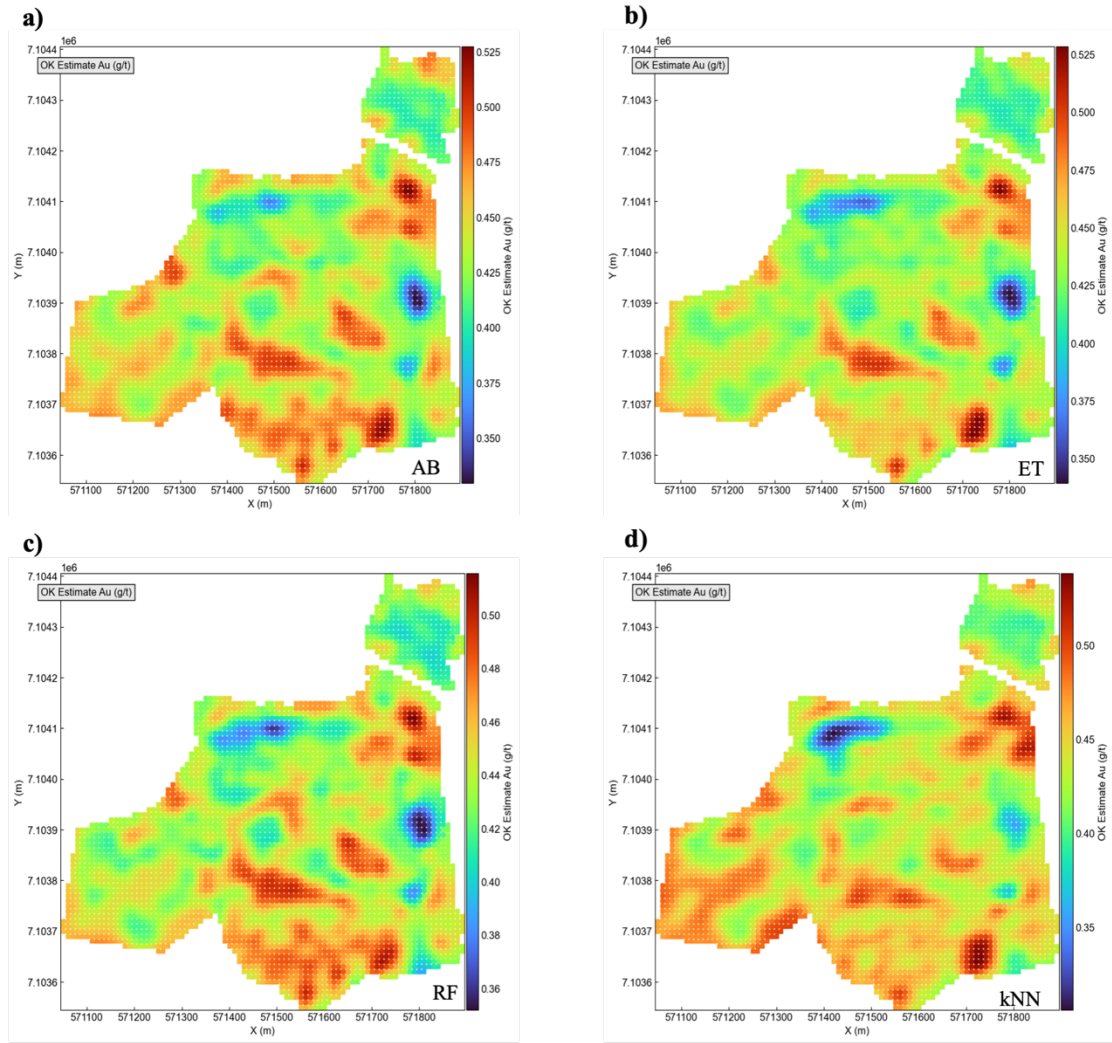


Figure 13. Visualization of OK gold grade estimates showing spatial variation in gold grades. (a) AB, (b) ET, (c) RF and (d) kNN.

To determine spatial continuity in the TSF, a semi-variogram analysis was performed for each ML model (Figure 14). The nugget effect is approximately 0.5 and shows continuity at the origin. The ellipses in the bottom right of each of the plots indicates anisotropy of the gold grades in the TSF in the major and minor directions (Appendix E).

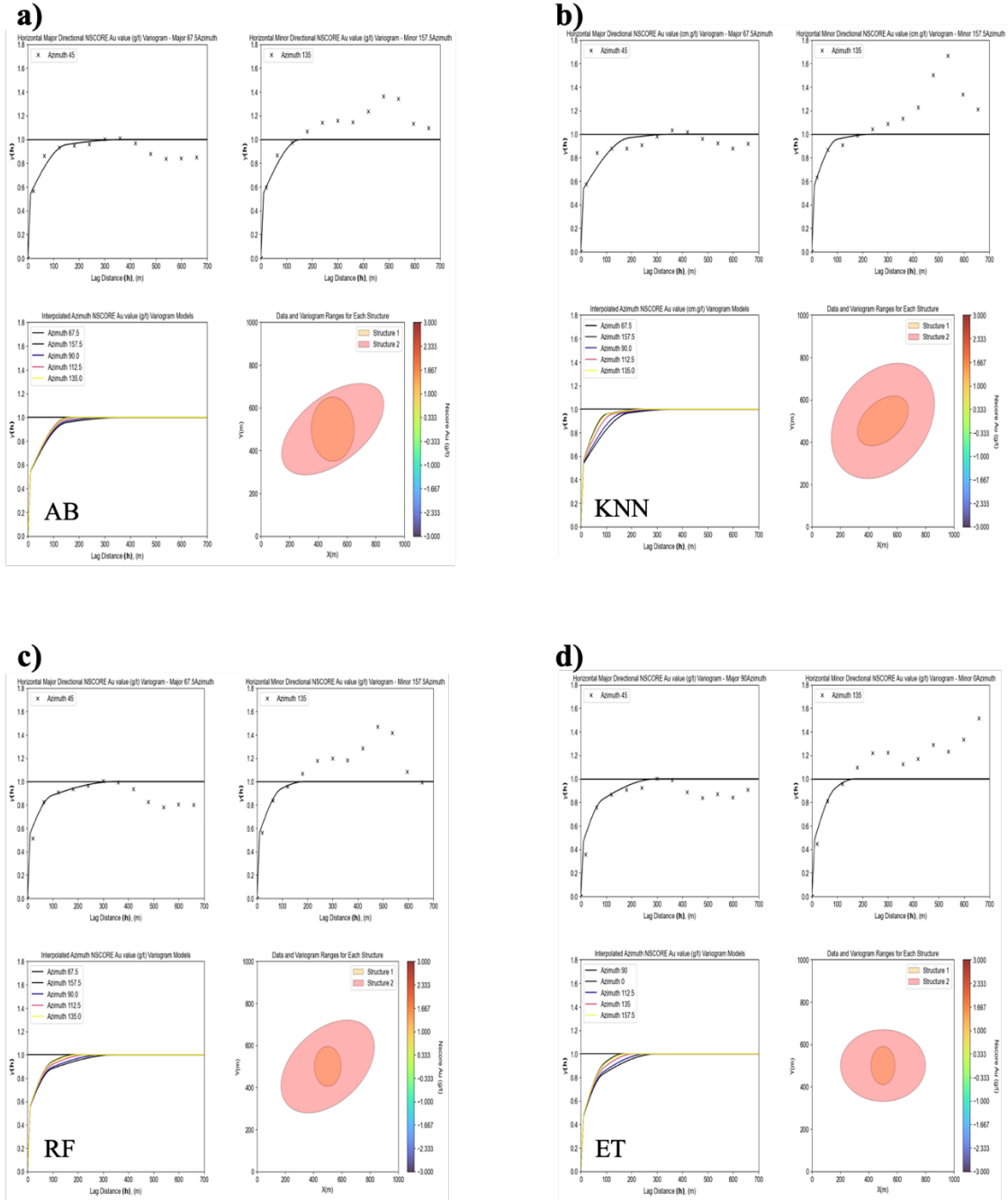


Figure 14. Experimental variogram with fitted variogram models. (a) AB, (b) kNN, (c) RF and (d) ET.

5.3. Sentinel-2 multi-spectral band decomposition for prediction of gold

AB had the highest CoD value between the training and test dataset. As such, it was used to show the reflectance response for gold in the TSF in five selected spectral bands. A quantitative comparison was made between spectral bands from one of the 17 Sentinel-2 images acquired for this research (Appendix B). The blue: band 2, green: band 3, red: band 4, visible to near infrared (VNIR): band 8 and shortwave infrared (SWIR): band 11 spectral bands of the Sentinel-2 image acquired on 4 October 2019 were used. The bands were selected based on their spatial resolution, the band wavelength and reduced noise levels. The spatial resolutions of the spectral bands are 10 metres for bands 2,3,4 and 8 and 20 metres for band 11. The OK gold grade estimates predicted using each of the spectral bands were compared with each other to determine the estimation correlation. A visual observation of the OK estimation maps for each spectral band (Figure 15) shows high gold grade estimations and high-grade gold zones in the TSF. Similar high grade gold clusters can be seen for bands 3,4,8 and 11 in Section 1A located left of the centre of the TSF with a north-south trend. This high-grade zone is absent in the band 2 OK estimation map. Similarly, in the Section 1A of the TSF north of the R41 road, medium gold grades dominate in the estimation maps for Bands 4,8 and 11, with more prominent higher grades in bands 8 and 11 estimation maps. The OK estimation map for Band 2 is dissimilar to the estimation maps for Bands 3, 4, 8 and 11. A cross-validation was done using the actual predicted gold grades using the band reflectance and the OK estimations. The CoD for each band is shown in Table 6 and Figure 16. The CoD values for each OK estimation using the five different bands shows that SWIR - band 11 had the highest value across all machine learning methods. The SWIR band showed higher correlation with gold in the TSF. A comparison of the actual gold grades with OK estimation shows that SWIR - band 11 had the least number of residuals with a symmetrical plot, indicating that the actual and the estimated gold grades correlated well with each other (Figure 17). Bands 2, 3, 4, and 8 all had similar residuals.

Table 6. CoD value for the comparison of the actual gold grade predictions and the OK estimations.

| Bands | CoD | | | |
|--------------|------------|-----------|------------|-----------|
| | AB | RF | kNN | ET |
| 2 | 0.9223 | 0.9102 | 0.9115 | 0.9117 |
| 3 | 0.9344 | 0.9364 | 0.9221 | 0.9219 |
| 4 | 0.9301 | 0.9407 | 0.929 | 0.9288 |
| 8 | 0.9335 | 0.9441 | 0.9339 | 0.9432 |
| 11 | 0.9591 | 0.9598 | 0.9591 | 0.9592 |

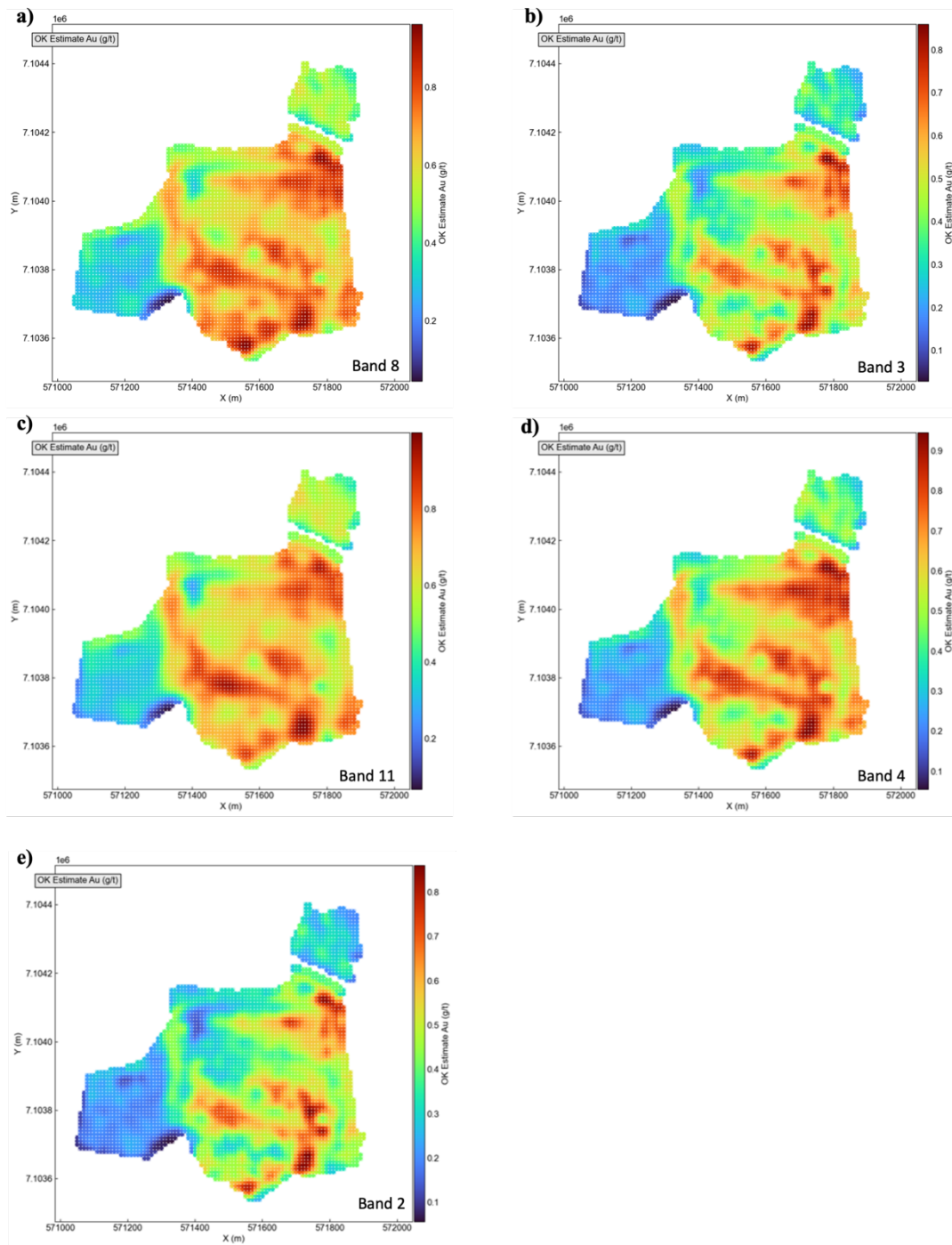


Figure 15. OK estimation maps for the five spectral bands selected. (a) Band 8, (b) Band 3, (c) Band 11 and (d) Band 4 and (e) Band 2.

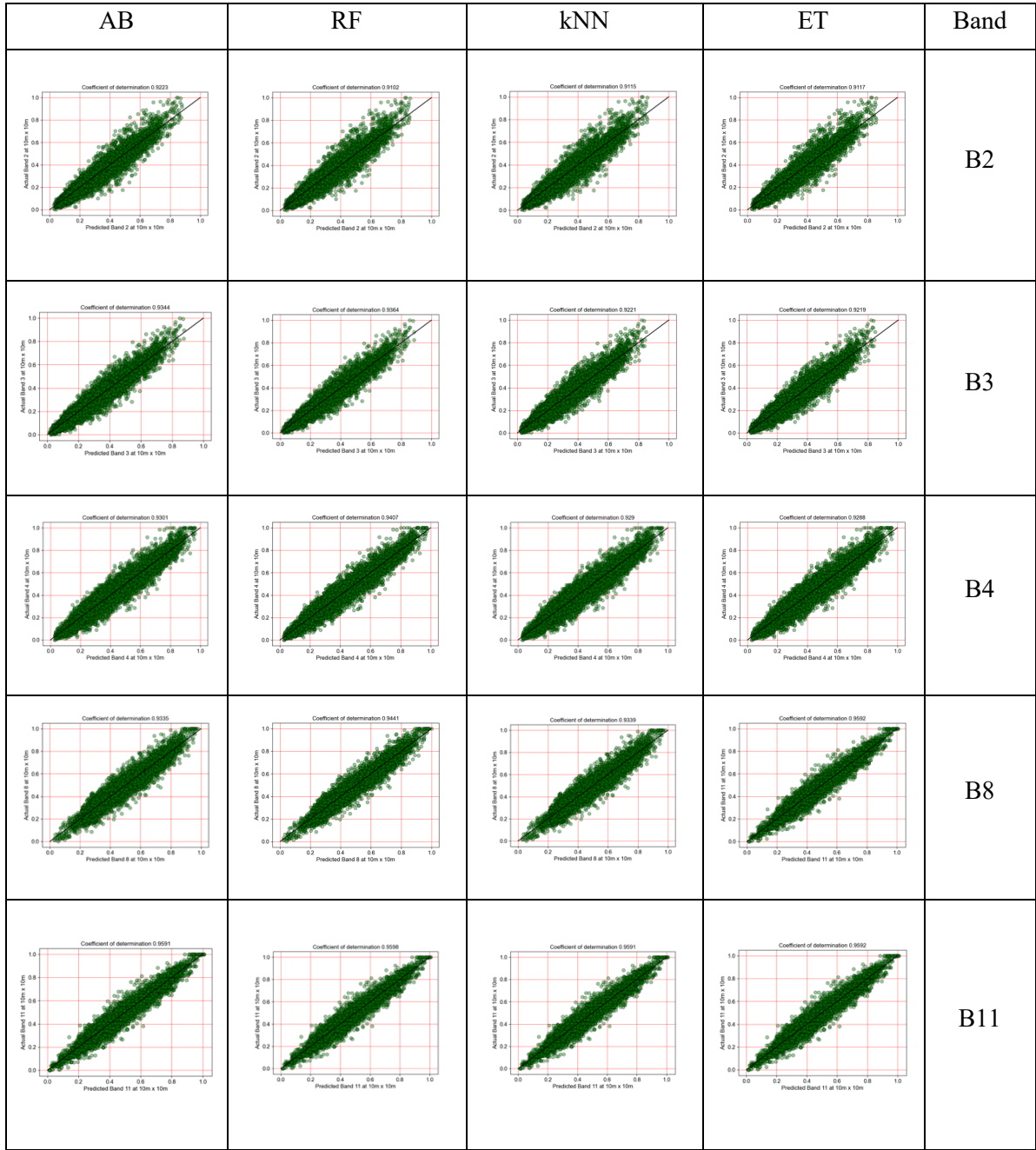


Figure 16. A comparison of the CoD plots for the predicted gold grades and the OK gold grade estimation

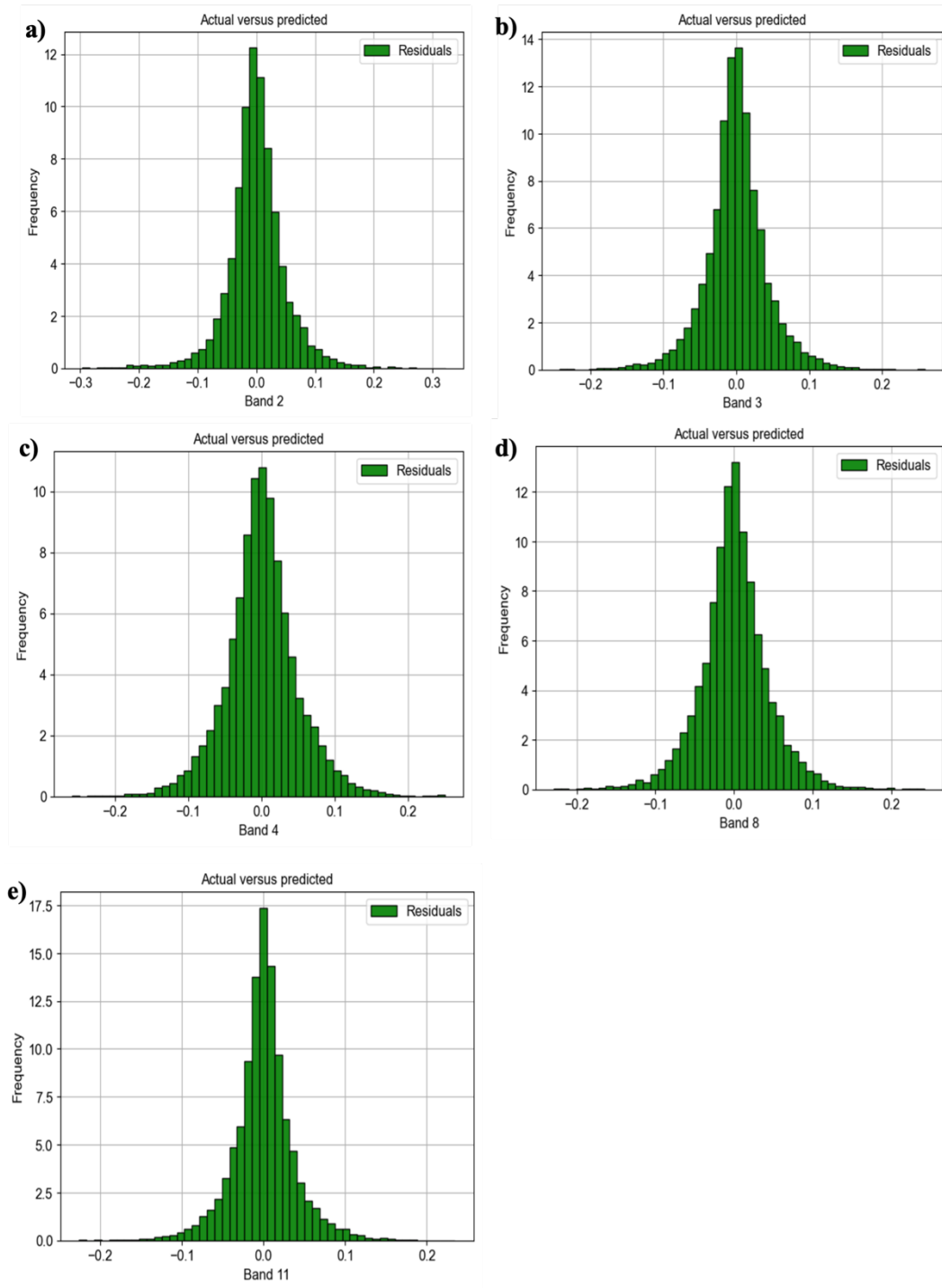


Figure 17. Plot of the residuals when comparing the actual and the predicted gold grades in the TSF.

6. Discussions

In this chapter, the results presented in Chapter 5 is discussed in the context of previous research in the field. This discussion cites the work of others to support and explain the observations presented in Chapter 5. Consideration for the implications of the results for the exploration of critical raw materials in TSFs with respect to securing CRM in Europe is also discussed.

6.1. Evaluation of prediction efficiency and accuracy

The prediction maps showed sections in the TSF with high gold grades. Section 1A of the TSF located north of the R41 road had high gold grade predictions for the Sentinel-2 satellite image acquired on 24 August 2015. The high-grade zone was observed in all the ML prediction maps but was not observed in the 2D geostatistical models. This is attributed to the time lag between the date when the image was acquired and the date when the borehole data was collected in 2013. The high-gold grades predicted by the ML models in this section of the TSF correlates to the high density of bore holes drilled, indicating the company was expecting high gold grades at that location. This high-grade zone was not observed in the 2D geostatistical models. This can be attributed to the section of the TSF being located below the low-grade surface tailing shown in the 2D geostatistical models. Furthermore, this indicates that as the time lapse continued, the low-grade surface tailing was removed to access the high-grade zone below which was observed in the satellite images acquired in from 2015 to 2016. This can be seen using the time lapse prediction maps (Figure 18).

Section 1A located north of the R41 road is the first section of the TSF exploited by the company. The ML models were able to predict gold in TSF at locations with known high-grade gold mineralisation. This high-grade zone was not observed in the 2D surface geostatistical model indicating that the mineralized zone was located greater than 10cm below the surface of the TSF. The 2D vertically averaged model which was expected to capture the vertical dimension of the TSF was unable to do so since this high-grade zone was clearly sampled in the borehole survey and was evident at the base of this zone in the 3D geostatistical block model (Appendix D). This agrees with the work of Zhang *et al.*, (2023b) that there is greater benefit in combining geochemical data and satellite imagery for the estimation of mineral resources in TSF. The combined use of geochemical data and remote sensing data to capture the vertical extent of the TSF is necessary given that remote sensing is a surface method. This can be an essential factor in the use of this methodology at locations such as the arctic circle where there is snow cover on the surface of the during the year.

The high-grade zone in Section 1A located in the southeastern section of the TSF is observed in the 2D geostatistical models but absent in the ML prediction maps. Based on the borehole positions in Figure 3, this zone was not sampled during the borehole survey. This high-grade zone can be attributed to extrapolation by the geostatistical model. Further observation shows a direct connection of this high-

grade gold zone with a low-grade gold zone trending from west to southeastern in Section 1A of the TSF. The high-resolution satellite image in Figure 19 shows disturbances in the TSF which can be attributed to remining of Section 1A of the TSF. This remining could have caused exposure of the lower sections of the TSF to rain and oxygen resulting in subsequent secondary gold mineralization. As more tailing containing sulphide minerals was exposed to oxygen and meteoric water it resulted in the production of acid mine drainage (AMD). In a TSF, factors such as weathering, rehabilitation and AMD redistributes various chemicals including target resources within the TSF Hansen (2015, 2018 cited in Nwaila *et al.*, 2021). AMD can cause the leaching, mobilisation and transport of minerals in TSF from regions with higher to lower pH values. This is supported by the work of Parviainen *et al.* (2020) who found that acidic leachates resulting from sulphide oxidation in the vadose zone of the TSF they studied dissolved the secondary iron (Fe) precipitates in cemented layers, possibly remobilizing trace elements in the ground water. The gold deposits in the Witwatersrand Basin are associated with uraninite pyrite (Frimmel, 2014). As the Fe is precipitated, the gold is liberated and becomes mobile. As such, AMD can be the contributing factor for the high-grade secondary mineralization in the Section 1A of the TSF.

The predictions from the training and test datasets had higher mean gold grade values when compared to the 2D geostatistical surficial model, with the latter also having lower mean gold grade when compared with the 2D vertically averaged geostatistical model. The 2D surficial geostatistical model was developed by dimensionality reduction and retained 63.65% of the original 3D model data (Zhang *et al.*, 2022a). This indicates that fewer datapoints were used for the gold grade estimations for the 2D surficial geostatistical model. The 2D vertically averaged geostatistical models had a higher mean gold grade than the 2D surficial model but was similar to the mean gold grade of the ML models (Appendix A). This is attributed to the vertically averaged 2D geostatistical model capturing greater depths of the TSF.

The Lindum TSF was constructed in the 1940s (Deswick Mining Consultants, 2014). TSFs are not homogeneous with multiple origins of spatial variability. These origins of spatial variability observed in TSFs can be chronologically categorized as 1) variability of the originating ore body; 2) deposition ordering and shuffling; and 3) post-deposition chemical redistribution (Nwaila *et al.*, 2021). As such, tailing stored in the TSF over time is subject to physical and chemical changes. This confirms to the work of (Deswick Mining Consultants, 2014) that reported that the high grades of gold in the TSF was found in Section 1A in the slimes. They further reported that the assay results from the borehole showed gold and uranium mineralization in the TSF, with varying grades for each section of the TSF. It was found that the gold mineralization was concentrated at the base of the main zone. They proposed that the gold had migrated to this zone due to gravitational settling which was attributed to rainwater infiltration. This confirms to the work of Parviainen *et al.* (2020) that found higher gold concentrations in deeper layers of the TSF they studied. They reported this was due to the gravitational deposition of heavier gold particles in the tailing slurry deposited in the tailing impoundment. As the gold mineralization undergoes physical and chemical changes in the TSF over time, the spatial distribution

of the gold is also changed. As such an assessment of spatial continuity using a semi-variogram analysis was done. The analysis indicates anisotropy of gold grades in all variogram plots indicating spatial continuity in the TSF.

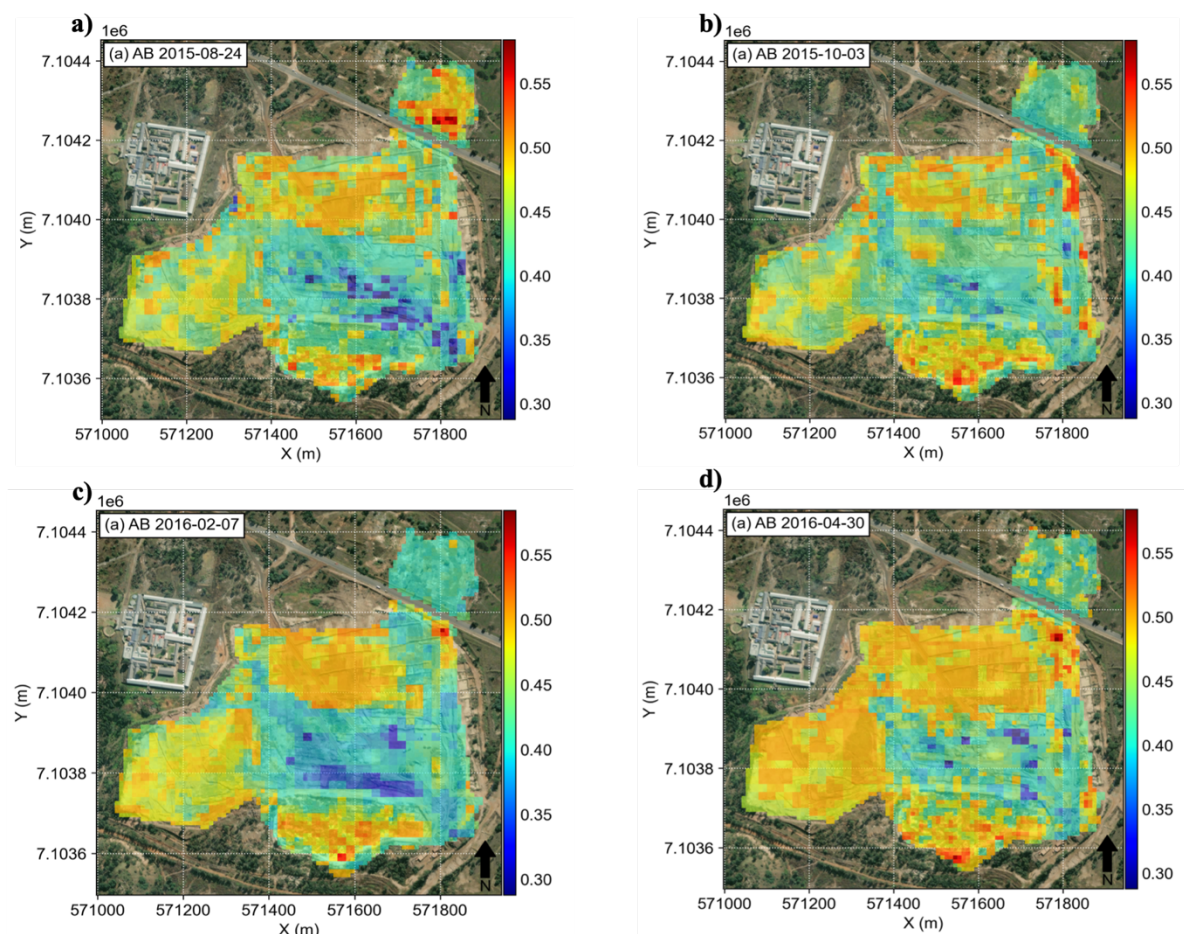


Figure 18. Prediction maps generated using AB ML model. Progressive mining of Section 1A shows the removal of the high-grade gold tailing.



Figure 19. Sentinel satellite image 6 January 2015.

6.2. Assessment of the suitability of machine learning algorithm for spatial predictive modeling of gold in TSFs

The use of ML methods has been shown useful in previous work for local and target exploration of conglomerate- hosted deposits (Nwaila *et al.*, 2020; 2022; Celik and Genc, 2021) and mineral prospecting (Rodriguez-Galiano *et al.*, 2015; Zhang *et al.*, 2022). The performance of the ML models was the basis for the selection of the best algorithm for predicting gold in the TSF. The ML algorithms can learn patterns and approximate complex nonlinear mapping and exploit the information contained in a dataset without assumption of data distribution (Zou, 2017).

The performance of the models showed that AB, ET and RF performed best when compared with kNN for predicting gold in the TSF. This confirms with the work of Zhang *et al.* (2023b); Boroh *et al.* (2022) who showed that RF outperformed kNN due to its advantage of depending solely on the actual data to determine predictions and Nwaila *et al.* (2022). RF, ET and AB being tree based or ensemble classifier and outperforming kNN further confirms with the work of Maxwell *et al.* (2018) who found that ensemble methods were more effective than methods that use a single classifier. The performance of RF and AB is based on the notion that a set of classifiers do perform better than an individual classifier (Rodriguez-Galiano *et al.*, 2012). However, the difference in the accuracies in predictions in RF and AB is attributed to how each method select the sample from which the decision is made. RF uses bagging while AB uses a random sampler. In bagging, each decision tree within the group which acts as a base estimator to establish the class label of an unlabelled instance is created by means of a sample with replacement from the training data (Ampomah, Qin and Nyame, 2020).

RF is a combination of tree predictors for which each tree depends on the values of a random vector sampled independently and with the same distribution for all trees in a forest of trees (Breiman, 2001). The decisions are made based on the weight of all the decisions each independent tree makes. In this method, since the decisions are made from the decisions of independent trees in the forest, each tree does not learn from the error made by other trees. AB does not use decision trees in the same sense as RF, in that, it uses stumps which are regarded as smaller trees in the decision-making process. As a decision is made, each stump learns from the error of the previous stump and adapts to making the new decision. Here, the decision-making process is not independent but the consideration of the decisions of other stumps are considered in the decision-making process. AB combines the output of weak regressors into weighted sum that represent the final output of the decision (Zhang *et al.*, 2021c). This makes AB models more robust than RF, hence its higher prediction accuracy. In their work, Zhang *et al.*, (2021c), found that when comparing algorithm selection and final testing AB and RF performed the predictions across all elements including REEs and chalcophiles.

6.3. Efficiency of multi-spectral remote sensing band in encoding spatial features and gold concentration

A visualization of the OK estimation maps of the five spectral bands clearly shows the reflectance values in the TSF. This indicates that all band amplitudes selected for the analysis were justified. The comparison of the CoD for the OK estimations for the five spectral bands using the four ML models, shows the SWIR - band 11 had the highest CoD values across all the ML models (Figure 16). This indicates that gold in the TSF had a good correlation with the SWIR - band 11. This confirms to the work of Rajendran and Nasir (2019) who showed that the SWIR, VNIR spectral bands of ASTER were useful for mapping of minerals and lithology. Remote sensing data have a depth penetration of approximately a few micrometres in the very near infrared wavelengths and only a few centimetres in the thermal infrared and microwave wavelengths (in hyper arid regions) (Rajesh, 2004).

The SWIR - band 11 had a higher CoD value. The VNIR bands also had high CoD values, indicating that the choice of spectral bands was not a major factor for the reflectance variations. Previous work by Zhang *et al.*, 2023b showed that gold grade increased with band amplitude in a non-linear relationship when the geochemical data and the remote sensing data were fused together. The plot of the histogram of prediction residuals showed symmetric histogram plots for all the spectral bands analysed indicating low variation in the predicted gold grades and the OK estimations in the spectral bands analysed. Further, this indicates that there is a low variation of what the ML model AB can explain. This correlates to the AB prediction model having a high CoD when its performance was measured.

7. Recommendations

The method explored in this research using satellite remote sensing and machine learning for mineral resource estimation in a defunct TSF can be explored further based on the results and the performance of the machine learning models. As such, the following are recommendations for future work:

1. The ML models used in this research can be deployed in iron ore TSFs located in Sweden, Europe where exploratory work is carried out to determine the valorisation potential of REEs. This can be done to determine the transferability of the models to TSF with different geochemical compositions. This recommended work must take into consideration the environmental conditions in Nordic countries such as fog, prolonged periods of snow cover in the winter months and the high reflectance values from snow and ice.
2. Extended research can be done to compare the use of Sentinel-2 satellite images with higher resolution multispectral images using the methodology applied in this research.
3. Further work can be done using unsupervised classification on the test TSF used in this research and the results compared to determine the performance of the two ML methods in predicting gold concentration in the TSF.
4. The development of a resource estimation workflow to standardize in-situ gold resource estimation using satellite remote sensing can be done based on this work.
5. Determination of mineral domains in the TSF through further vertical extension of the depth dimension.

8. Conclusion

The aim of this research was to explore the use of remote sensing and machine learning to characterise gold in a defunct TSF. The current demand for critical raw materials in Europe is increasing. With the EU having little to no primary ore deposits of CRMs such as REEs and phosphorous, the use of defunct TSF can serve as a secondary source of these CRMs in Europe. With current iron ore mines owned by Swedish mining companies already exploring ways to recover CRM from TSF and the large number of defunct TSF in Europe, exploiting TSF can move Europe closer to meeting increasing demands for CRMs.

The results of the study were consistent with the aim and objectives, that remote sensing and machine learning can be used to predict gold in a defunct TSF. ML algorithms were used to build prediction models which were trained on data from one TSF and tested on a TSF derived from mining gold in the Witwatersrand Basin in South Africa. The deployment of the ML models on a different TSF showed there was replicability and generality of the models used in the research. In this sense, the models used on the TSF in South Africa can be deployed on a TSF in Europe to make predictions for gold and CRMs.

The ML models were effective at predicting gold in the TSF when compared to the use of traditional OK to develop the 2D and 3D geostatistical models. The accuracy of the ML models was excellent on the training and testing sets indicating that the models performed excellently in predicting gold in the TSF. The mean gold grade predicted by the ML models was 0.4 g/t, corresponding to similar gold grade in the 2D vertically averaged geostatistical model with 0.4 g/t. Gold in the TSF was predicted by training models based on AB, RF, kNN and ET. The results showed that AB, ET and RF prediction models performed the best in predicting gold. The SWIR – band 11 at spatial resolution 20 showed higher correlation with gold in the TSF.

The advantage of the method proposed in this research for mineral resource estimation is that Sentinel-2 satellite images are free and requires less time to develop a resource model in comparison to costly borehole surveys. This method however has limitations. One limitation is that remote sensing is useless in areas with substantial overburden such as vegetation or water (Zhang et al., 2023b), snow cover and fog during the winter months as is the case of Nordic countries such as Sweden, Norway and Finland. As such, careful choice of the type of remote sensing data used must maximise desirable land coverage where necessary (Zhang *et al.*, 2023b). In this case there is need for innovation to meet this challenge given the benefits of using satellite imagery and ML for mineral resource estimation in defunct TSF. In addition to this, remote sensing can be inadequate when used alone for mineral resource estimation in TSFs. As such, supplementing the use of remote sensing with geochemical data can add value to the dataset in the vertical dimension and the mineral resource estimation. Other limitation to the use of the methodology proposed in this research is the absence of circularity in mining operations. As a circular approach to doing business, there is more scope for the methods proposed in this research. With a focus on resource supply and considering the factors that affect circularity of CRM such as: 1)

production ceilings; 2) decreases in reserves; 3) changes in the production ratio of bigger to smaller deposit; 4) inefficient price systems and 5) increases in extraction cost (Overland, 2019, cited in Nwaila *et al.*, 2021a), there can be a shift in the demand for CRM and hence the use of the proposed methodology.

9. Acknowledgements

The successful completion of my research project would not have been possible without the cooperation of a number of individuals to whom I owe much gratitude. Firstly, I would like to thank my Lord Jesus Christ for my life and for bringing me this far.

I would like to express my sincere gratitude to my supervisors, Prof. Dr. Glen Nwaila and Dr. Pauline Jeanneret and mentor, Dr. Steven Zhang and Dr. Julie E. Bourdeau (Geological Survey of Canada), and Ms. Janine Fleming (Sibanye-Stillwater) for all their valuable constructive criticism, suggestions, insights, friendship, and patience in the course of this research project. I am also grateful to the SINReM Board for giving me the opportunity to complete this research and my masters' degree.

My family and friends have been a pillar of strength and support for me during this very challenging period. I thank you for your encouragement, help, prayers, and counsel. To my parents, Orin and Sharon Agard who did not receive the opportunity of a university education, I dedicate this master's thesis to you. Thank you for your encouragement and teachings on life that kept me going.

10. References

- Agangi, A., Hofmann, A., Rollion-Bard, C., Marin-Carbonne, J., Cavalazzi, B., Large, R. and Meffre, S. (2015). Gold accumulation in the Archaean Witwatersrand Basin, South Africa—Evidence from concentrically laminated pyrite. *Earth-Science Reviews*, 140, pp.27-53.
- Akbar, D.A. (2012). Reserve estimation of central part of Choghart north anomaly iron ore deposit through ordinary kriging method. *International Journal of Mining Science and Technology*, 22(4), pp.573-577.
- Ampomah, E.K., Qin, Z. and Nyame, G. (2020) “Evaluation of Tree-Based Ensemble Machine Learning Models in Predicting Stock Price Direction of Movement,” *Information*, 11(6), p. 332. Available at: <https://doi.org/10.3390/info11060332>.
- Berry, M.W., Mohamed, A. and Yap, B.W. eds. (2019). Supervised and unsupervised learning for data science. *Springer Nature*.
- Boroh, A.W., Lawou, S.K., Mfenjou, M.L. and Ngounouno, I. (2022). Comparison of geostatistical and machine learning models for predicting geochemical concentration of iron: case of the Nkout iron deposit (south Cameroon). *Journal of African Earth Sciences*, 195, p.104662.
- Breiman, L. (2001). Random forests. *Machine learning*, 45(1), pp.5-32.
- Government of Canada (2015) Pre-processing. Available at: <https://www.nrcan.gc.ca/maps-tools-and-publications/satellite-imagery-and-air-photos/tutorial-fundamentals-remote-sensing/image-interpretation-analysis/pre-processing/9403> [5 November 2022].
- Celik, T. and Genc, B., 2021. A Comparative Study on Machine Learning Algorithms for Geochemical Prediction Using Sentinel-2 Reflectance Spectroscopy. *Journal of Mining and Environment*, 12(4), pp.987-1001.
- David, M. (2012). *Geostatistical ore reserve estimation*. Elsevier.
- Deswick Mining Consultants. (2014). Competent Persons Report on Lindum Reefs Slimes Dumps - Resource Model (DMC20800 rev 1.0).
- Deutsch, C.V. and Journel, A.G. (1992). Geostatistical software library and user's guide. *Oxford University Press*, 8(91), pp.0-1.
- Dumakor-Dupey, N.K. and Arya, S. (2021). Machine Learning—A Review of Applications in Mineral Resource Estimation. *Energies*, 14(14), p.4079.
- Durand, J.F. (2012). The impact of gold mining on the Witwatersrand on the rivers and karst system of Gauteng and North West Province, South Africa. *Journal of African Earth Sciences*, 68, pp.24-43.
- El Bouchefry, K. and de Souza, R.S. (2020). Learning in big data: Introduction to machine learning. In *Knowledge discovery in big data from astronomy and earth observation* (pp. 225-249). *Elsevier*.
- Europa.eu. (2020). *Critical Raw Materials Resilience: Charting a Path towards Greater Security and Sustainability. Communication from the Commission to the European Parliament, the Council, the European Economic and Social Committee and the Committee of the Regions*. [online] Available at: <https://eur-lex.europa.eu/legal-content/EN/TXT/?uri=CELEX:52020DC0474>. [15 October 2022]

Frimmel, H.E. (2005). Archaean atmospheric evolution: evidence from the Witwatersrand gold fields, South Africa. *Earth-Science Reviews*, 70(1-2), pp.1-46.

Frimmel, H.E. (2014). A giant Mesoarchean crustal gold-enrichment episode: Possible causes and consequences for exploration.

Ge, G., Shi, Z., Zhu, Y., Yang, X. and Hao, Y. (2020). Land use/cover classification in an arid desert-oasis mosaic landscape of China using remote sensed imagery: Performance assessment of four machine learning algorithms. *Global Ecology and Conservation*, 22, p.e00971.

Ghorbani, Y., Nwaila, G.T., Zhang, S.E. and Hay, M.P. (2021). Repurposing legacy metallurgical data part II: Case studies of plant performance optimisation and process simulation. *Minerals Engineering*, 160, p.106667.

Ghorbani, Y., Nwaila, G.T., Zhang, S.E., Hay, M.P., Bam, L.C. and Guntoro, P.I. (2020). Repurposing legacy metallurgical data Part I: A move toward dry laboratories and data bank. *Minerals Engineering*, 159, p.106646.

Ghorbani, Y., Nwaila, G.T. and Chirisa, M., 2022. Systematic framework toward a highly reliable approach in metal accounting. *Mineral Processing and Extractive Metallurgy Review*, 43(5), pp.664-678.

Gold one international limited. (2013). Gold one international limited. (2013, May). *Integrated environmental impact assessment and environmental management programme*. [online] Gold one international limited. Available at: https://sahris.sahra.org.za/sites/default/files/additionaldocs/Lindum_Dumps_-_EIA%20EMP%202013_05_28%20Final%20Report%20for%20DWA.pdf [Accessed 20 December 2022].

Hunt, G.R. (1977). Spectral signatures of particulate minerals in the visible and near infrared. *Geophysics*, 42(3), pp.501-513.

John, V. et al. (2016) “Real-Time Lane Estimation Using Deep Features and Extra Trees Regression,” *Image and Video Technology*, pp. 721–733. Available at: https://doi.org/10.1007/978-3-319-29451-3_57.

Kasmaeeyazdi, S., Mandanici, E., Balomenos, E., Tinti, F., Bonduà, S. and Bruno, R. (2021). Mapping of Aluminum Concentration in Bauxite Mining Residues Using Sentinel-2 Imagery. *Remote Sensing*, 13(8), p.1517.

Kinnunen, P.H.M. and Kaksonen, A.H. (2019). Towards circular economy in mining: Opportunities and bottlenecks for tailings valorization. *Journal of Cleaner Production*, 228, pp.153-160.

Kotsiantis, S.B., Zaharakis, I. and Pintelas, P. (2007). Supervised machine learning: A review of classification techniques. *Emerging artificial intelligence applications in computer engineering*, 160(1), pp.3-24.

Kuhn, M. and Johnson, K. (2013). *Applied predictive modeling* (Vol. 26, p. 13). New York: Springer.

Lamamra, A., Neguritsa, D.L. and Mazari, M. (2019), November. Geostatistical modeling by the Ordinary Kriging in the estimation of mineral resources on the Kieselguhr mine, Algeria. In *IOP Conference Series: Earth and Environmental Science* (Vol. 362, No. 1, p. 012051). IOP Publishing.

Lary, D.J., Alavi, A.H., Gandomi, A.H. and Walker, A.L. (2016). Machine learning in geosciences and remote sensing. *Geoscience Frontiers*, 7(1), pp.3-10.

Liang, S. and Wang, J. eds. (2019). Advanced remote sensing: terrestrial information extraction and applications. *Academic Press*.

Lottermoser, B.G. (2010). *Sulfidic mine wastes*. In *Mine wastes* (pp. 43-117). Springer, Berlin, Heidelberg.

Matheron, G. (1963). Principles of geostatistics. *Economic geology*, 58(8), pp.1246-1266.

Maxwell, A.E., Warner, T.A. and Fang, F. (2018). Implementation of machine-learning classification in remote sensing: An applied review. *International Journal of Remote Sensing*, 39(9), pp.2784-2817.

Mulenshi, J., Gilbricht, S., Chelgani, S.C. and Rosenkranz, J. (2021). Systematic characterization of historical tailings for possible remediation and recovery of critical metals and minerals–The Yxsjöberg case. *Journal of Geochemical Exploration*, 226, p.106777.

Nwaila, G.T., Zhang, S.E., Bourdeau, J.E., Ghorbani, Y. and Carranza, E.J.M. (2022). Artificial intelligence-based anomaly detection of the Assen iron deposit in South Africa using remote sensing data from the Landsat-8 Operational Land Imager. *Artificial Intelligence in Geosciences*, 3, pp.71–85. doi:10.1016/j.aiig.2022.10.001.

Nwaila, G.T., Ghorbani, Y., Zhang, S.E., Frimmel, H.E., Tolmay, L.C., Rose, D.H., Nwaila, P.C. and Bourdeau, J.E. (2021a). Valorisation of mine waste-Part I: Characteristics of, and sampling methodology for, consolidated mineralised tailings by using Witwatersrand gold mines (South Africa) as an example. *Journal of Environmental Management*, 295, p.113013.

Nwaila, G.T., Ghorbani, Y., Zhang, S.E., Tolmay, L.C., Rose, D.H., Nwaila, P.C., Bourdeau, J.E. and Frimmel, H.E. (2021b). Valorisation of mine waste-Part II: Resource evaluation for consolidated and mineralised mine waste using the Central African Copperbelt as an example. *Journal of Environmental Management*, 299, p.113553.

Nwaila, G.T., Zhang, S.E., Frimmel, H.E., Manzi, M.S., Dohm, C., Durrheim, R.J., Burnett, M. and Tolmay, L., 2020. Local and target exploration of conglomerate-hosted gold deposits using machine learning algorithms: a case study of the Witwatersrand gold ores, South Africa. *Natural Resources Research*, 29, pp.135-159.

Parviainen, A., Soto, F. and Caraballo, M.A. (2020). Revalorization of Haveri Au-Cu mine tailings (SW Finland) for potential reprocessing. *Journal of Geochemical Exploration*, 218, p.106614.

Rajesh, H.M. (2004). Application of remote sensing and GIS in mineral resource mapping-An overview. *Journal of mineralogical and Petrological Sciences*, 99(3), pp.83-103.

Rajendran, S. and Nasir, S. (2019). ASTER capability in mapping of mineral resources of arid region: A review on mapping of mineral resources of the Sultanate of Oman. *Ore Geology Reviews*, 108, pp.33-53.

Rico, M., Benito, G., Salgueiro, A.R., Díez-Herrero, A. and Pereira, H.G. (2008). Reported tailings dam failures: a review of the European incidents in the worldwide context. *Journal of hazardous materials*, 152(2), pp.846-852.

Rodriguez-Galiano, V.F., Ghimire, B., Rogan, J., Chica-Olmo, M. and Rigol-Sanchez, J.P. (2012). An assessment of the effectiveness of a random forest classifier for land-cover classification. *ISPRS journal of photogrammetry and remote sensing*, 67, pp.93-104.

Taberima, S., Junaedi, E., Sarwom, R., Lindongi, L.E. and Mulyanto, B. (2020). The acid mine drainage (AMD) impact of tailings and non-tailings on the ecosystem changes in the ModADA sedimentation area, Timika. *Journal of Degraded and Mining Lands Management*, 7(2), p.2085.

www.usgs.gov. (2018). *USGS EROS Archive - Sentinel-2* | U.S. Geological Survey. [online] Available at: https://www.usgs.gov/centers/eros/science/usgs-eros-archive-sentinel-2?qt-science_center_objects=0 [Accessed 20 December. 2022].

www.sgu.se. (2021). *Critical raw materials*. [online] Available at: <https://www.sgu.se/en/mineral-resources/critical-raw-materials/>. [04 November 2022].

www.sgu.se. (2020). *Mines and environmental impact*. [online] Available at: <https://www.sgu.se/en/mineral-resources/mines-and-environmental-impact/>. [Accessed 20 December 2022].

Zabcic, N., Rivard, B., Ong, C. and Müller, A. (2014). Using airborne hyperspectral data to characterize the surface pH and mineralogy of pyrite mine tailings. *International Journal of Applied Earth Observation and Geoinformation*, 32, pp.152-162.

Zhang, S.E., Bourdeau, J.E., Nwaila, G.T. and Corrigan, D. (2021a). Towards a fully data-driven prospectivity mapping methodology: A case study of the Southeastern Churchill Province, Québec and Labrador. *Artificial Intelligence in Geosciences*, 2, pp.128–147. doi:10.1016/j.aiig.2022.02.002.

Zhang, S.E., Nwaila, G.T., Bourdeau, J.E. and Ashwal, L.D. (2021b). Machine learning-based prediction of trace element concentrations using data from the Karoo large igneous province and its application in prospectivity mapping. *Artificial Intelligence in Geosciences*, 2, pp.60-75.

Zhang, S.E., Agard, S., Nwaila, G.T., Bourdeau, J.E., Ghorbani, Y., Carranza, E.J.M. (2023a). Transfer learning based on spatiotemporal remote sensing and big data geochemistry for evaluating mineral resources in tailing storage facilities (**currently in the process of being published**)

Zhang, S.E., Glen T. Nwaila, G.T., Bourdeau, J.E., Ghorbani, Y., Carranza, E.J.M. (2023b). Towards Big Geochemical Data from High-Resolution Remote Sensing Data via Machine Learning: Application to a Tailing Storage Facility in the Witwatersrand Goldfields (**currently in the process of being published**).

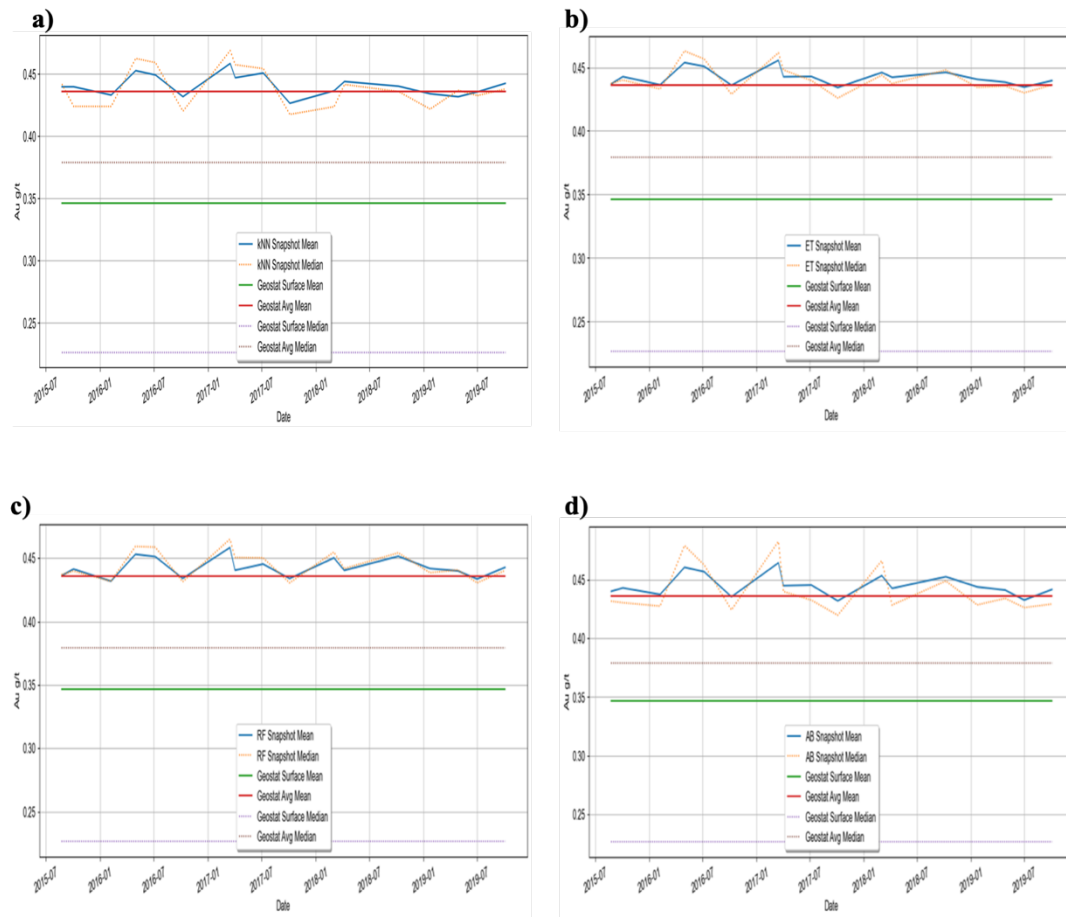
Zheng, L. and Xu, W. (2021). An improved adaptive spatial preprocessing method for remote sensing images. *Sensors*, 21(17), p.5684.

Zerzour, O., Gadri, L., Hadji, R., Mebrouk, F. and Hamed, Y. (2021). Geostatistics-Based Method for Irregular Mineral Resource Estimation, in Ouenza Iron Mine, Northeastern Algeria. *Geotechnical and Geological Engineering*, 39(5), pp.3337-3346.

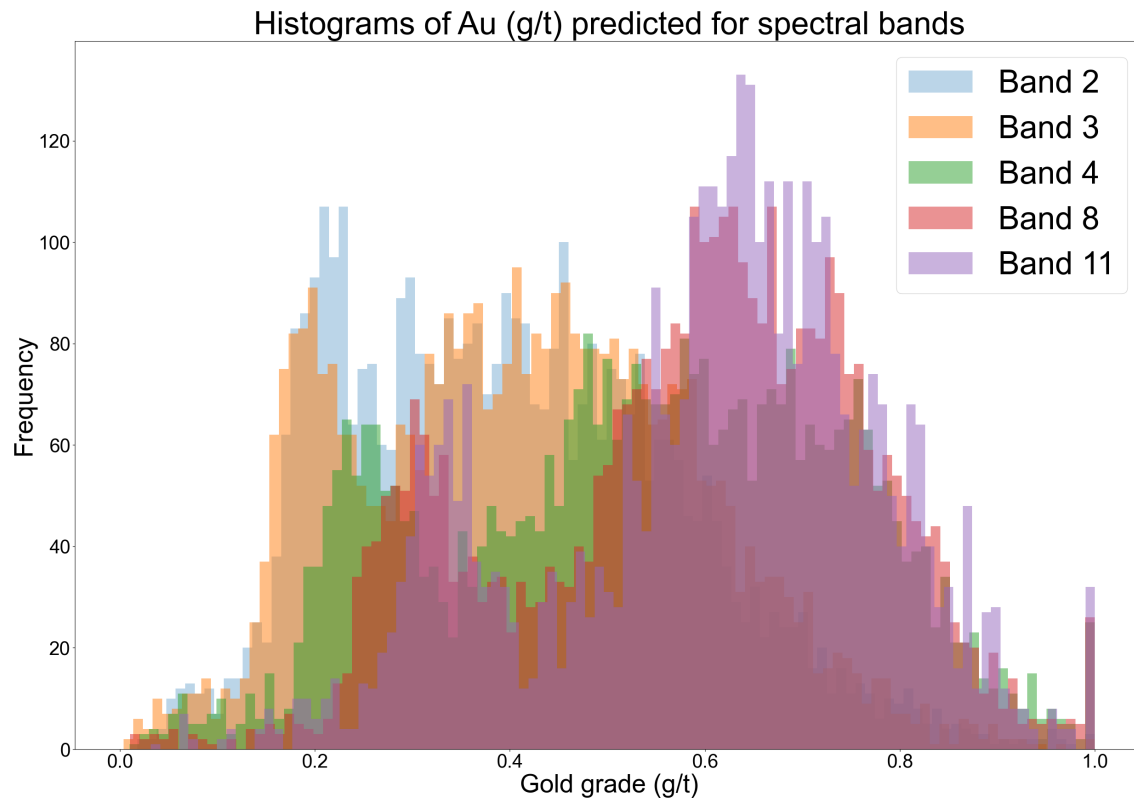
Zuo, R. (2017). Machine learning of mineralization-related geochemical anomalies: A review of potential methods. *Natural Resources Research*, 26(4), pp.457-464.

Appendices

Appendix A. Descriptive statistics plot for the resource models. (a) kNN, (b) ET, (c) RF and (d) AB.



Appendix B. Histogram and descriptive statistics plot for reflectance in spectral bands 2, 3, 4, 8 and 11.



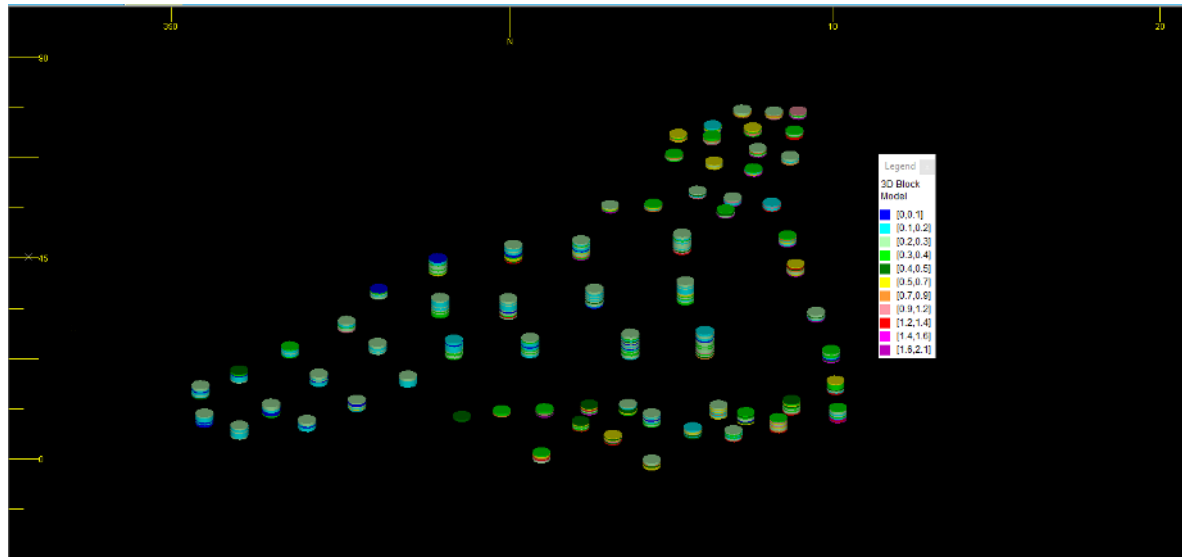
Descriptive statistics of the spectral bands analysed.

| | Band 2 | Band 3 | Band 4 | Band 5 | Band 8 | Band 11 |
|--------------|--------|--------|--------|--------|--------|---------|
| count | 4048.0 | 4048 | 4048 | 4048 | 4048 | 4048 |
| mean | 0.4 | 0.4 | 0.5 | 0.5 | 0.6 | 0.6 |
| std | 0.2 | 0.17 | 0.21 | 0.19 | 0.18 | 0.18 |
| min | 0.01 | 0.00 | 0.01 | 0.01 | 0.01 | 0.03 |
| 25% | 0.3 | 0.3 | 0.4 | 0.4 | 0.5 | 0.5 |
| 50% | 0.4 | 0.4 | 0.5 | 0.6 | 0.6 | 0.6 |
| 75% | 0.5 | 0.5 | 0.7 | 0.7 | 0.7 | 0.7 |
| max | 1.0 | 1.0 | 1.0 | 1.0 | 1.0 | 1.0 |

Appendix C. Machine learning algorithms prediction parameters.

| | Element | Size Fraction | Method | Call | CoD | Parameters | Model Name |
|---|---------|---------------|--------|-------------------------|--------------------|--|------------|
| 0 | Au | 1.0 | kNN | KNeighborsRegressor() | 0.701401812159353 | {'n_neighbors': 3, 'weights': 'distance'} | Au_kNN |
| 1 | Au | 1.0 | RF | RandomForestRegressor() | 0.8745026989851363 | {'max_depth': 25, 'max_features': 8, 'min_samples_leaf': 1, 'min_samples_split': 6, 'n_estimators': 1500} | Au_RF |
| 2 | Au | 1.0 | ET | ExtraTreesRegressor() | 0.9208181160917104 | {'max_depth': 27, 'max_features': 9, 'min_samples_leaf': 1, 'min_samples_split': 2, 'n_estimators': 1000} | Au_ET |
| 3 | Au | 1.0 | AB | AdaBoostRegressor() | 0.9501923639580201 | {'base_estimator': DecisionTreeRegressor(max_depth=26, max_features=6, min_samples_leaf=2, min_samples_split=3), 'base_estimator__max_depth': 26, 'base_estimator__max_features': 6, 'base_estimator__min_samples_leaf': 2, 'base_estimator__min_samples_split': 3, 'n_estimators': 500} | Au_AB |

Appendix D. 3D Block model showing boreholes drilled in Lindum TSF.



Appendix E. Variogram maps for bands 2, 3, 4, 8 and 11 using AB predictions.

